APPENDIX H

ALCOVE 8–NICHE 3 TESTING AND PRETEST PREDICTIONS (RESPONSE TO RT 3.05, SDS 3.01 AIN-1, AND USFIC 6.03)

Note Regarding the Status of Supporting Technical Information

This document was prepared using the most current information available at the time of its development. This Technical Basis Document and its appendices providing Key Technical Issue Agreement responses that were prepared using preliminary or draft information reflect the status of the Yucca Mountain Project's scientific and design bases at the time of submittal. In some cases this involved the use of draft Analysis and Model Reports (AMRs) and other draft references whose contents may change with time. Information that evolves through subsequent revisions of the AMRs and other references will be reflected in the License Application (LA) as the approved analyses of record at the time of LA submittal. Consequently, the Project will not routinely update either this Technical Basis Document or its Key Technical Issue Agreement appendices to reflect changes in the supporting references prior to submittal of the LA.

APPENDIX H

ALCOVE 8–NICHE 3 TESTING AND PRETEST PREDICTIONS (RESPONSE TO RT 3.05, SDS 3.01 AIN-1, AND USFIC 6.03)

This appendix provides a response for Key Technical Issue (KTI) Agreements Radionuclide Transport (RT) 3.05, Structural Deformation and Seismicity (SDS) 3.01 Additional Information Needed (AIN)-1, and Unsaturated and Saturated Flow under Isothermal Conditions (USFIC) 6.03. These agreements relate to (1) the documentation of the Alcove 8–Niche 3 (also referred to as Niche 3107) testing and predictive modeling for the unsaturated zone, (2) the fracture-informed observation of infiltration and seepage related to observed fracture patterns, and (3) the responses to NRC staff comments on the Alcove 8–Niche 3 tests and pretest predictions.

H.1 KEY TECHNICAL ISSUE AGREEMENTS

H.1.1 RT 3.05, SDS 3.01, and USFIC 6.03

Agreement RT 3.05 was reached during the U.S. Nuclear Regulatory Commission (NRC)/U.S. Department of Energy (DOE) Technical Exchange and Management Meeting on Radionuclide Transport held December 5 to 7, 2000, in Berkeley, California (Reamer and Williams 2000a). During the course of this meeting, RT Subissue 3, Radionuclide Transport through Fractured Rock, was discussed, and agreement RT 3.05 was reached.

Agreement SDS 3.01 was reached during the NRC/DOE Technical Exchange and Management Meeting on Structural Deformation and Seismicity held October 11 to 12, 2000, in Las Vegas, Nevada (Reamer and Gil 2000). The agreement was reached during the course of this meeting in the discussion of SDS Subissue 3, Fracturing and Structural Framework.

Agreement USFIC 6.03 was reached during the NRC/DOE Technical Exchange and Management Meeting on Unsaturated and Saturated Flow under Isothermal Conditions held August 16 and 17, 2000 in Berkeley, California (Reamer and Williams 2000b). During the course of this meeting, USFIC Subissue 6, Matrix Diffusion, was discussed, and agreement USFIC 6.03 was reached.

The wording of the three agreements is as follows:

RT 3.05

> Provide the documentation for the Alcove 8/Niche 3 testing and predictive modeling for the unsaturated zone. DOE will provide documentation for the Alcove 8/Niche 3 testing and predictive modeling for the unsaturated zone in updates to the AMRs In Situ Field Testing of Processes and Radionuclide Transport Models Under Ambient Conditions, both available to the NRC in FY 2002.

SDS 3.01

> The Enhanced Characterization of the Repository Block (ECRB) long-term test and the Alcove 8 Niche 3 test need to be "fracture-informed" (i.e., observation of seepage needs to be related to observed fracture patterns). Provide documentation which discusses this aspect. DOE responded that for the passive test, any observed seepage will be related to full periphery maps and other fracture data in testing documentation. The documentation will be available by any potential license application (LA). For Niche 3, fracture characterization is completed and a 3-D representation will be included in testing documentation. The documentation will be available August, 2001.

In response to the SDS 3.01 agreement, the DOE on September 18, 2001, provided a letter regarding a three-dimensional depiction of fractures between Alcove 8 and Niche 3 (Brocoum 2001a). Subsequently, the DOE provided NRC staff with a document about the process and methodology for developing the three-dimensional depiction of fractures between Alcove 8 and Niche 3 on November 19, 2001 (Williams 2001). After reviewing these documents, the NRC issued SDS 3.01 AIN-1 (Schlueter 2002).

The wording of the SDS 3.01 AIN-1 is as follows:

SDS 3.01 AIN-1

> The NRC staff requests the documentation to show how, or the methodology to ensure that, actual or expected hydrologic and transport test results were or will be interpreted in light of fracture-fault patterns and lithostratigraphic information in the test volume vicinity.

USFIC 6.03

> The DOE will complete the Alcove 8 testing, taking into consideration the NRC staff comments, if any, and document the results in a DOE-approval AMR, due date: May 2001.

H.1.2 Related Key Technical Issue Agreements

KTI agreements RT 3.05 and USFIC 6.03 relate to KTI agreements RT 3.06 and SDS 3.02 in that the four agreements involve the documentation of Alcove 8–Niche 3 tests and pretest predictions.

The Alcove 8–Niche 3 tests involve the two-phase seepage and tracer tests in the fault test and two-phase seepage and tracer tests in the large-plot test. The first-phase tracer test for the large-plot test is still ongoing. For the fault test, the DOE provided the *Pre-Test Prediction for Alcove 8-Niche 3 Crossover Test* on March 12, 2001 (Brocoum 2001b) and *Updated Pre-Test Prediction of Tracer Transport for Alcove 8–Niche 3 Cross-Over Fault Test* (Phase I) on June 27, 2002 (Ziegler 2002). For the large-plot test, the DOE has provided the resolution for KTI agreements RT 3.06 and SDS 3.02 in Appendix E of this technical basis document.

NRC staff provided review comments on the testing and pretest predictions for the fault test (Reamer 2002; Schlueter 2003). The NRC requested that the DOE address eight review comments of NRC staff in its response to RT 3.05, SDS 3.01, and USFIC 6.03 (Schlueter 2003). Responses to agreements RT 3.05, SDS 3.01, and USFIC 6.03 are provided below.

H.2 RELEVANCE TO REPOSITORY PERFORMANCE

RT 3.05 and USFIC 6.03 relate to the DOE providing documentation on the Alcove 8–Niche 3 tests and pretest prediction on seepage and tracer transport and responses to the NRC staff review comments on the related documents the DOE has provided.

The seepage and transport testing in the Alcove 8–Niche 3 tests provides one of the few opportunities to collect in situ data to confirm unsaturated zone transport parameters and validate unsaturated zone conceptual models for flow and transport. The mesoscale (21 m in depth) Alcove 8–Niche 3 tests provide confidence on the understanding for the flow and transport processes and the total system performance assessment. The mesoscale tests are related to site-scale processes of infiltration and percolation with drift-scale processes of capillarity, diversion, and seepage.

Agreements RT 3.05 and USFIC 6.03 are relevant to repository performance because capillarity and water diversion around the drift observed in the tests are important mechanisms reducing seepage into the waste emplacement drifts. The observed mesoscale percolation and transport processes in the tests are also related to the total system performance assessment because the test results are relied upon for building confidence in the understanding of mountain-scale unsaturated flow and radionuclide transport processes in fractured rock and for validation of unsaturated zone process models.

H.3 RESPONSE

The information in this report is responsive to agreements RT 3.05 and USFIC 6.03 made between the DOE and the NRC and responsive to AIN request SDS 3.01 AIN-1. Planned testing at Alcove 8–Niche 3 has evolved since August 2000 and is still ongoing. However, DOE has obtained sufficient testing and modeling results to address these agreements. Thus, the report contains the information that DOE considers necessary for NRC review for closure of these agreements.

H.3.1 Fault and Large-Plot Tests

The Alcove 8–Niche 3 tests were performed to evaluate unsaturated zone flow, seepage response, and matrix diffusion processes. These tests consist of the fault test and the large-plot test with different phases and stages, as shown in Table H-1. Alcove 8 was excavated into the wall of the Enhanced Characterization of Repository Block (ECRB) Cross-Drift, while Niche 3 was excavated into the wall of the Exploratory Studies Facility (ESF) main drift in close proximity to the crossover point of the two drifts. The fault test (Phase-I seepage and tracer tests and Phase-II seepage test with reduced infiltration rates) was completed, while the large-plot test, which has two test phases, is still ongoing. In the fault test, liquid (with or without tracers) was released into a narrow trench along a minor fault, and in the large-plot test, liquid was released into a plot of 3 m by 4 m into a fracture network on the floor of Alcove 8. The seepage and

breakthrough curves of tracers, if used, were monitored at the niche ceiling. The wetting-front migration was monitored using a number of boreholes. The *Pre-Test Prediction for Alcove 8-Niche 3 Crossover Test* (Brocoum 2001b) and *Updated Pre-Test Prediction of Tracer Transport for Alcove 8–Niche 3 Cross-Over Fault Test* (Phase I) for the fault test (Ziegler 2002) have been provided. The pretest prediction for seepage in Stages 2 and 3 and tracer transport in Stage 3 for Phase I of the large-plot test is provided in Appendix E of this technical basis document. This prediction for the large-plot test was based on the infiltration and seepage data collected in Stage 1 of Phase I. This appendix (Appendix H) documents responses to NRC review comments on the pretest predictions for the fault test and the fracture-informed analysis of infiltration and seepage observations in Stage 1 (from August 20, 2002, to March 24, 2003) of Phase I of the large-plot test.

Table H-1. Description of the Fault and Large-Plot Tests with Different Phases (Phases I and II) and Stages (Stages 1, 2, and 3)

	Fault Test			Large-Plot Test		
Phase	Test Conditions	Infiltration/ Seepage Test	Tracer Test	Test Conditions	Infiltration/ Seepage Test	Tracer Test
I	Ponded Condition	3/1/2001 to 4/7/2002	10/1/2001 to 4/7/2002	Ponded Condition	Stage 1: 8/20/2002 to 3/24/2003 (with 12 plots)	Stage 1: No Tracer Test
					Stage 2: 3/24/2003 to 8/4/2003 (with 2 plots)	Stage 2: No Tracer Test
					Stage 3: 8/4/2003 – ? (with 12 plots)	Stage 3: Tracer Test (ongoing)
II	Nonponded Condition	4/8/2002 to 8/20/2002	No Tracer Test	Planned	Planned	Planned

Section H.4.2 provides an analysis of the infiltration and seepage observed in Phase I (Stage 1) of the large-plot test.

H.3.2 U.S. Nuclear Regulatory Commission Review Comments

To meet the closure requirement for KTI Agreement USFIC 6.03, the responses to eight review comments made by the NRC staff on the Alcove 8–Niche 3 testing and pretest predictions are provided (Reamer 2002; Schlueter 2003). Supporting discussions for some of the comments can be found in other responses to related KTI agreements, as indicated below.

H.3.2.1 Comment 1

The DOE should provide a complete description of the actual tests by including physical dimensions, experimental set-up, and initial conditions, such that NRC staff could identify the tests to which the pretest predictions apply.

Response: The complete description of the Alcove 8–Niche 3 large-plot test is presented in Section H.4.1, including geometric and geologic settings and experiment setup. The experiment settings for the fault test are documented in *In Situ Field Testing of Processes* (BSC 2003a).

H.3.2.2 Comment 2

The DOE needs to justify its use of a continuum model when the spacing of flowing fractures exceeds the grid size.

Response: Justification for the continuum approach at the scale of the seepage model grid has been documented in *Seepage Calibration Model and Seepage Testing Data* (BSC 2004) and by Finsterle (2000). The continuum approach appropriately captures in-fracture-plane flow diversion, which is the dominant mode of flow diversion in fracture rock. The detailed justification is documented in Appendix D of this technical basis document.

H.3.2.3 Comment 3

The DOE should address the NRC's concern about the usefulness of comparisons between predicted and observed results without a mass balance of water and on the water mass lost due to evaporation.

Response: The water mass lost due to evaporation during the test period was small. The applied water from permeameters evaporated into Alcove 8 or infiltrated into underlying fractured rock. The infiltrated water (1) was stored within the fractured rock between Alcove 8 and Niche 3, (2) was diverted around the niche and flowed out of the system from the horizon of the niche floor, or (3) seeped into the niche. The seeped water was collected by the seepage capture system or evaporated into the niche. To reduce the effects of evaporation, the infiltration plot on the alcove floor was covered and separated from the rest of the alcove. Evaporation from the infiltration plot was almost zero so that the liquid-release rate from permeameters was equal to the infiltration rate through the large plot. To minimize the effects of evaporation resulting from the main drift ventilation, the bulkhead door at the entrance to Niche 3 was closed and sealed during the test period and the measured relative humidity within the niche was between 90% and 100%. Therefore, the water mass lost due to evaporation during the test period was small. Mass-balance issues at the Alcove 8–Niche 3 test bed and in Niche 5 (also referred to as Niche 1620) are addressed in Appendix C of this technical basis document.

H.3.2.4 Comment 4

The DOE needs to clarify the basis for the use of calibrated drift-scale rock property values as an initial estimate for the calibration of the fault test and to give the rationale for using the values, while more recent and representative rock properties are available to run predictive simulations.

Response: The basis for using calibrated drift-scale rock properties as initial estimates for calibrating the numerical model for the fault test was that these rock properties represent the mean values for the drift scale, which is closer to the test-site scale than the 1-ft scale used for measuring air permeabilities (i.e., more recent and representative rock properties). The numerical model was calibrated using the measured seepage rate and waterfront transport time, and site-specific rock properties were obtained (Williams 2001). Based on the calibrated rock

properties, the pretest prediction for tracer breakthrough curves was made. In model calibration, the most important information specific to the fault-testing site was the measured seepage and travel-time. The air-permeability data available in a number of boreholes in the niche and under the alcove floor were used in the model calibration to constrain the fracture permeability range; no site-specific data for other rock properties (e.g., parameters for capillary force strength) were available. Section H.4.3 presents the methods for use of rock property information in model calibration for the large-plot test pretest prediction, in which similar calibration procedures were used. Therefore, the basis for the use of calibrated drift-scale rock properties was the consideration of scale-dependent permeability.

H.3.2.5 Comment 5

Clarification is needed on how the effects from previously saturated fractures will be considered when evaluating the fracture-matrix interface area, or give the rationale for why these effects need not be considered.

Response: The previously saturated fractures had little effect on estimating the fracture–matrix interface area. The fracture-matrix interface area was evaluated by tracer tests in both the fault and large-plot tests. Tracers were introduced into the test system during a relatively stable-infiltration time period. For the fault test, the Phase-I tracer test was conducted from October 1, 2001 to April 8, 2002, while the Phase-I infiltration and seepage test was conducted from March 6, 2001 to April 8, 2002. The infiltration rate was relatively stable from mid-May 2001, to the tracer test completion. No sharp changes in fracture saturation occurred for the entire tracer test. For the ongoing large-plot tracer test, which started at a time when infiltration rate was relatively stable, the change in the fracture-matrix interface area was also small. In addition, the active fracture model was used in the numerical model to capture the preferential flow. In the active fracture model, the fracture activity (percentage of active fractures in the total connected fractures) varied with saturation, and change in interface area for flow from fractures to the matrix was captured in the active fracture model. Therefore, the previously saturated fractures had little effect on estimating the fracture-matrix interface area.

H.3.2.6 Comment 6

A rationale is needed for the assumption that fracture-matrix interaction mechanisms are the same for a flow system with increasing or decreasing saturation.

Response: In the active fracture model used in the pretest prediction, the methodology for calculating the flow from fractures to the matrix is different than that for the flow from the matrix to fractures. As indicated by Liu et al. (1998), different fracture-matrix interface-area reduction factors are used to calculate flow and transport processes for the different flow directions. During a wetting time period, flow direction is from fractures to the matrix, and the fracture-matrix interface area reduction factor is used. During the drying time, water flows from the matrix to fractures, and no reduction for the interface area is used.

H.3.2.7 Comment 7

The DOE needs to address the NRC staff's concern about the possibility of sequential Phase II test interference consisting of a state of disequilibrium due to the rapidity of the sequence of tests.

Response: To avoid the potential effects of disequilibrium or test interference, the tracer was introduced after flow processes were stabilized, as evidenced by stable infiltration and seepage rates for each phase of the tests. The fracture-relative permeability and fracture-matrix interface area for tracer tests remained relatively unchanged because they were calibrated using the data collected during the stabilized flow period. In the fault test, the tracer test was conducted in Phase 1 when water flow was stabilized. No tracer test was involved in Phase II. In the large-plot test, tracers were released in Stage 3 of Phase I when the unsaturated flow was stabilized. For flow only, the transient flow under varying infiltration rates can be captured in the numerical model because no equilibrium conditions were assumed for the flow interaction between fractures and the matrix. The Multiple Interacting Continuum (MINC) approach was used for numerical simulation of the transient variably saturated flow to capture the steep hydraulic gradients at the interfaces between the fractures and the matrix.

H.3.2.8 Comment 8

The DOE should describe all features, events, and processes observed in Alcove 8–Niche 3 tests.

Response: Many physical processes occurred during the infiltration, seepage, and tracer tests. In Section H.4.2, an assessment is given for each feature, event, and process occurring in the Alcove 8–Niche 3 large-plot test.

H.3.3 Fracture-Informed Analysis of Observed Infiltration and Seepage

To meet the closure requirements for SDS 3.01 AIN-1, the fracture-informed analysis of observed infiltration and seepage was conducted using the fracture data available, including the fracture maps on the alcove floor and niche ceiling and the fracture data from full-periphery geologic maps and detailed line survey of the ESF main drift and the ECRB Cross-Drift. The spatial and temporal variability in observed infiltration and seepage was analyzed considering fracture density, fracture connectivity, large fracture and small fracture clusters, and fracture orientation. An analysis was conducted to correlate observed infiltration and seepage to the fracture density of the infiltration subplot and seepage collection tray units, respectively. Section H.4.2 presents the fracture-informed assessment.

Section H.4.3 also shows that geologic information was adequately captured in the hydrologic models associated with the Alcove 8–Niche 3 tests (BSC 2003a).

H.4 BASIS FOR THE RESPONSE

This appendix focuses on analysis of infiltration and seepage observed in Stage 1 of Phase I of the large-plot test. The fault test is not included in this section because it was documented in *In Situ Field Testing of Processes* (BSC 2003a).

H.4.1 Test Settings and Experiment Setup

An infiltration and seepage test was conducted at a 21 m scale (mesoscale) in deep, unsaturated fractured rock at Yucca Mountain, Nevada (BSC 2003a). Water was injected into a large plot on the floor of an alcove (Alcove 8) excavated on the side of the ECRB Cross-Drift. Seepage was collected in a niche (Niche 3), which was excavated into the wall of the ESF main drift and is located directly under the large infiltration plot. The large-plot test investigated the spatial and temporal variabilities in the unsaturated flow in fractured rock in terms of infiltration and seepage rates. The test also investigated the roles of fractures and the fracture network in transporting water in unsaturated, fractured rock.

H.4.1.1 Geometric and Geologic Settings

The ESF main drift and the ECRB Cross-Drift provide underground access to the hydrogeologic units of welded tuff above the horizon of the repository. Niche 3 is located in close proximity to the crossover point of the ESF main drift and the ECRB Cross-Drift (see Figure H-1). Niche 3 is a small drift of approximately 4 m in width and 6.3 m in length. The height of the niche ceiling varies, stepping from 3.25 m at the opening to 2.5 m towards the midpoint of the niche above the niche floor (BSC 2003a). The average elevation of the niche ceiling is 1,073.2 m. The total surface area of the niche ceiling is about 16.4 m^2.

Alcove 8 was excavated from the ECRB Cross-Drift to a position immediately above Niche 3 so that the mesoscale drift-to-drift test could be conducted at this location. Alcove 8 is wider and longer than Niche 3, covering the entire area of the niche ceiling. The elevation of the alcove floor is at 1,094.3 m, with the distance from the alcove floor to the niche ceiling about 21.1 m. The test system is within the unsaturated flow zone approximately 250 m below the ground surface.

This test system is located within the Topopah Spring welded tuff unit (TSw). Alcove 8 is situated within the upper lithophysal (Tptpul) subunit of the TSw unit. The Tptpul contains large naturally occurring cavities called lithophysae. Lithophysae cavities at the test site range from 0.5 to 0.75 m in length and 0.2 to 0.3 m in height. The majority of fractures appear to be cooling features associated with lithophysae cavities. These fractures resulted primarily from halos and rinds around the cavities. Short fractures link the cavities and rinds, resulting in a large overall average permeability for the entire network. The cavities and fractures in the Tptpul subunit lead to large effective fracture porosity (BSC 2003a). The calibrated porosity for the fault test conducted in the same system is 6.6%, which is much larger than the effective porosity of 1.0% in the middle nonlithophysal (Tptpmn) subunit. Niche 3 is situated within the Tptpmn subunit, a densely welded, highly fractured devitrified zone containing no lithophysal cavities. The contact interface between the two hydrogeologic subunits is at an elevation of 1,079.8 m, with a contact surface approximately horizontal in the testing area.

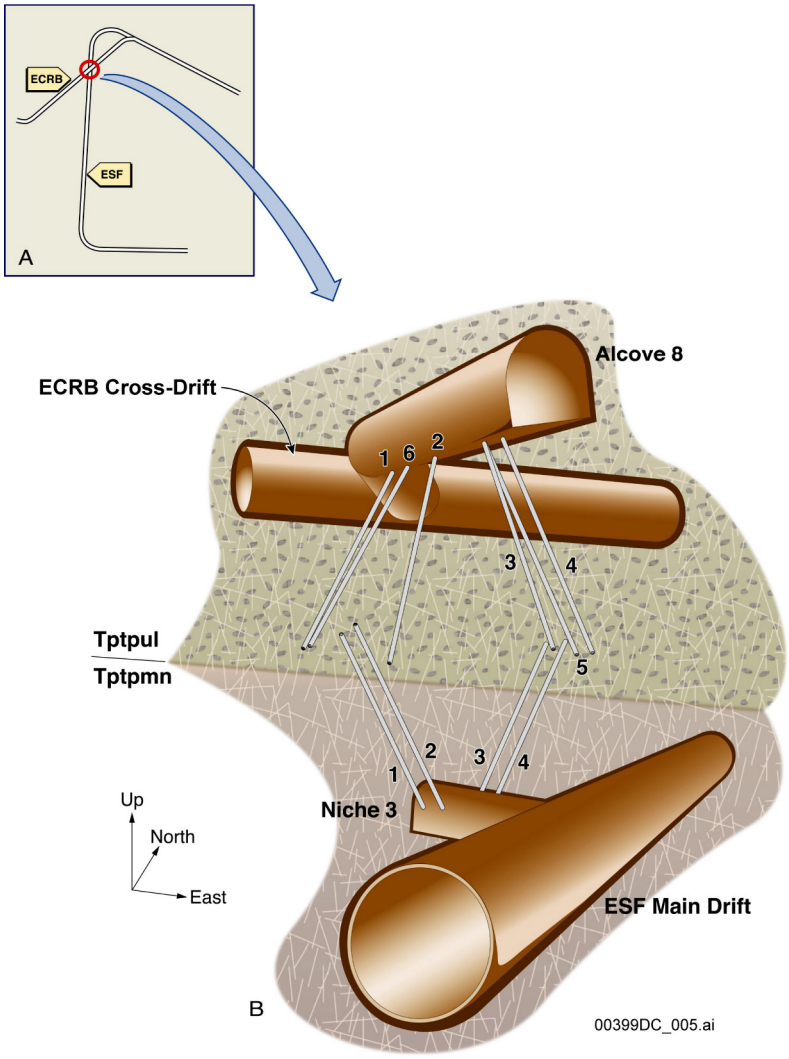

Source: BSC 2003a, Figure 6.12.1-2.

Figure H-1. Schematic Illustration of the Test Bed for the Large-Plot Infiltration and Seepage Test in the Alcove 8–Niche 3 System

The two hydrogeologic subunits consist of compositionally similar, moderately to densely welded ash-flow tuff. However, these units exhibit different fracture geometric characteristics (Hinds et al. 2003). The characteristics were determined based on data collected from underground excavations, borehole structure logs, and surface mapping studies. The best and most abundant data for fractures came from full-periphery geologic maps and a detailed line survey of the ESF main drift and the ECRB Cross-Drift. Within the Tptpul unit (upper unit), fracture frequency varies significantly, with a mean and standard deviation of 0.81 ±1.03 per meter (BSC 2003b; BSC 2003c). The fracture trace length for the upper unit is also highly variable in space (CRWMS M&O 2000). Variability in fracture frequency and trace length was also obtained within the Tptpmn unit (lower unit). Mean and standard deviation of fracture frequency are 4.32 ±3.41 per meter. The fracture trace length was calculated using fractures longer than 1.0 m while small fractures were not used. The small fractures longer than 0.3 m but less than 1.0 m were mapped only in a 3 km segment of the ESF main drift. The trace-length

distribution of the surveyed fractures for this segment showed that the fracture trace length varies from 0.3 m to 10.0 m (Hinds et al. 2003, Figure 5).

Matrix characteristics are fairly homogeneous within these two units (Flint 1998; Hinds et al. 2003).

H.4.1.2 Testing Site-Specific Fracture Characteristics

The fracture characteristics specific to the testing site are particularly important to analyzing test results because of their strong spatial variability. To accurately represent the fracture network at the testing site, the U.S. Geological Survey (USGS) mapped fractures on the floor of Alcove 8 and the ceiling of Niche 3. Only large, natural fractures longer than 1.0 m were surveyed; excavation-induced fractures and small fractures were excluded in these maps. Figure H-2 shows the fracture map with approximate configurations of 12 infiltration subplots for Alcove 8. Twenty-four long fractures can be identified on the map, with two different fracture sets intersecting (almost perpendicularly) in terms of the fracture strike. Most fractures share a similar dip in a range between 68° and 88°. The fracture frequency calculated based on the map is 1.03 per meter, which is similar to the mean value for the Tptpul subunit (BSC 2003d, Section 7.6).

As shown in Figure H-3, four major fractures pass through the central area of the niche ceiling along the niche axis. Intersecting the four long fractures are a number of short fractures, also on the ceiling of the niche. The calculated fracture frequency is about 1.72 per meter, and the fracture spacing is 0.58 m (BSC 2003d, Section 7.6). The fracture frequency calculated for the testing site is much less than that for the entire Tptpmn subunit, indicating that Niche 3 is located in a moderately fractured zone, as shown in the fracture density contour map by Wang and Bodvarsson (2003, Figure 3c).

Although the mapped fractures on the alcove floor and niche ceiling are not sufficient to represent the complicated fracture network between the two boundary surfaces, USGS generated a three-dimensional fracture network to depict the complicated fractures at the testing site (see Figure H-4). The generation was based on the mapped fractures on the two surfaces. In the generation process, trace-lengths of mapped fractures were used to project fracture planes into three dimensions; the trace lengths of individual fractures were used as the distance to populate projected fractures in the vertical dimension; fractures were depicted as square planes with the size of mapped fractures. However, fractures in the field exhibit strong spatial variabilities in fracture trace length and fracture frequency, as well as fracture orientations (strike and dip). These variabilities make the generated fracture network highly uncertain in terms of fracture connectivity. Considering that the generated fracture network was one of many stochastic realizations resulting from the high variabilities, the generated fracture network is not used in the modeling analysis of the test and in the fracture-informed analysis of observed seepage and infiltration rates.

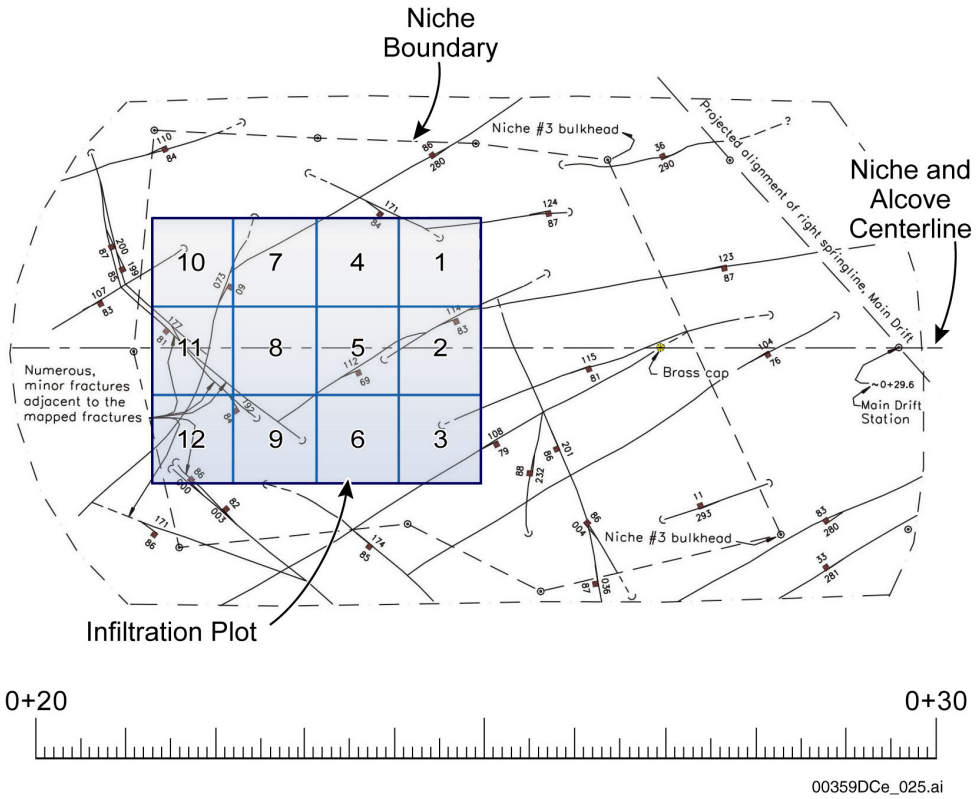

Source: DTNs: GS030108314224.001 (for the fracture map) and GS030608312242.005 (referring the notebook pages with Infiltration plot configuration and numbering information).

NOTE: The infiltration plot (drawn based on its planned outline in the fracture map) depicted in this figure is not exactly 3 m by 4 m.

Figure H-2. Fracture Map on the Floor of Alcove 8 with Approximate Configurations of the 12 Infiltration Subplots Used in the Large-Plot Test

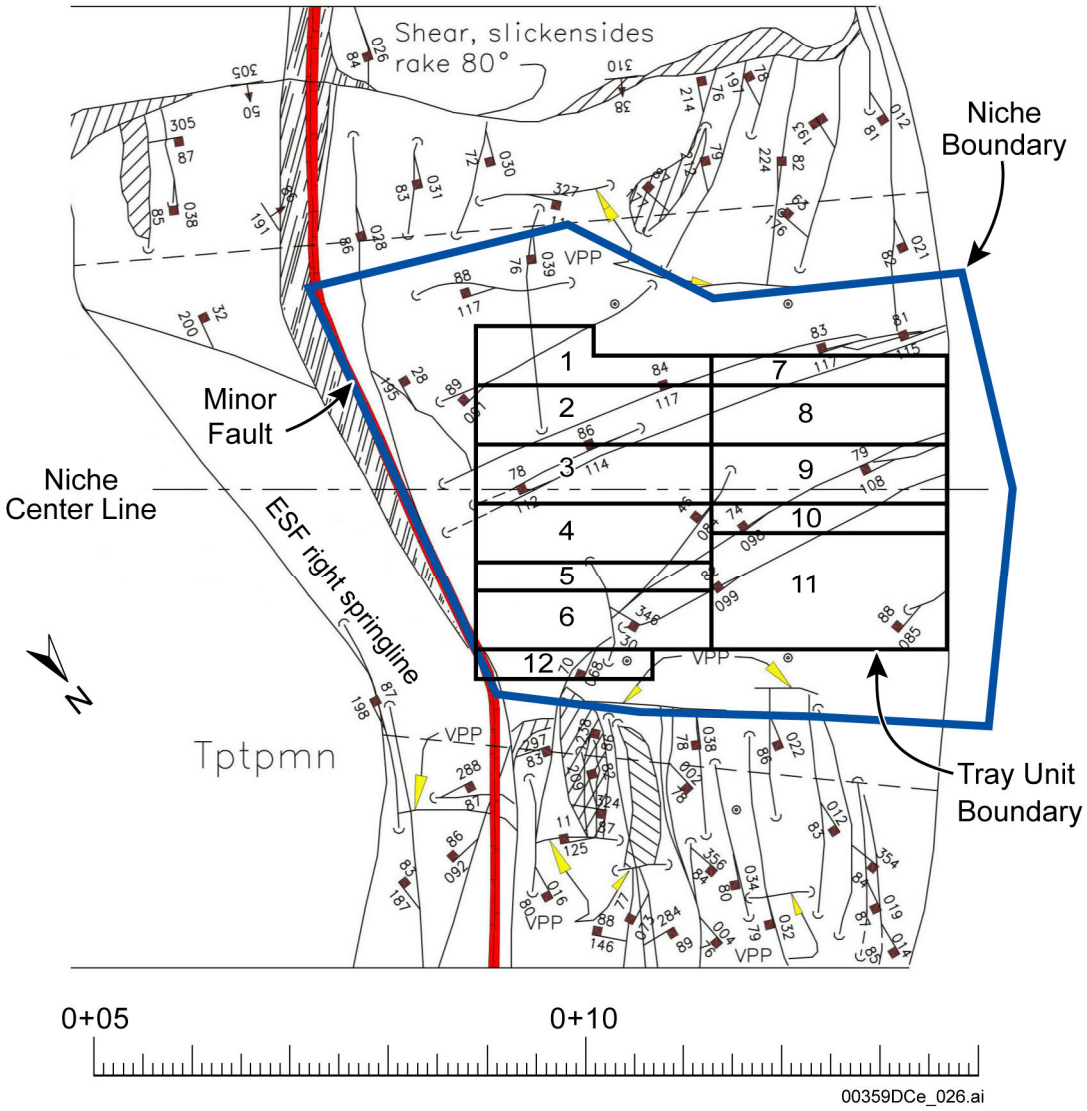

Source: DTNs: GS030108314224.001 (for the fracture map) and LB0306A8N3LIQR.001 (referring the notebook pages with tray configuration information).

NOTE: The correspondence between the above-tray unit numbering and the real numbering is 1 (U4-B2), 2 (U4-B3), 3 (U4-B4), 4 (U3-B2), 5 (U3-B3), 6 (U3-B4), 7 (U4-B1), 8 (U1-B5), 9 (U1-B4), 10 (U1-B3), 11 (U1-B1), and 12 (U3-B5).

Figure H-3. Fracture Map on the Ceiling and Sidewalls of Niche 3 with the Boundary of Niche Floor and Approximate Configurations of Tray Units of the Seepage Capture System

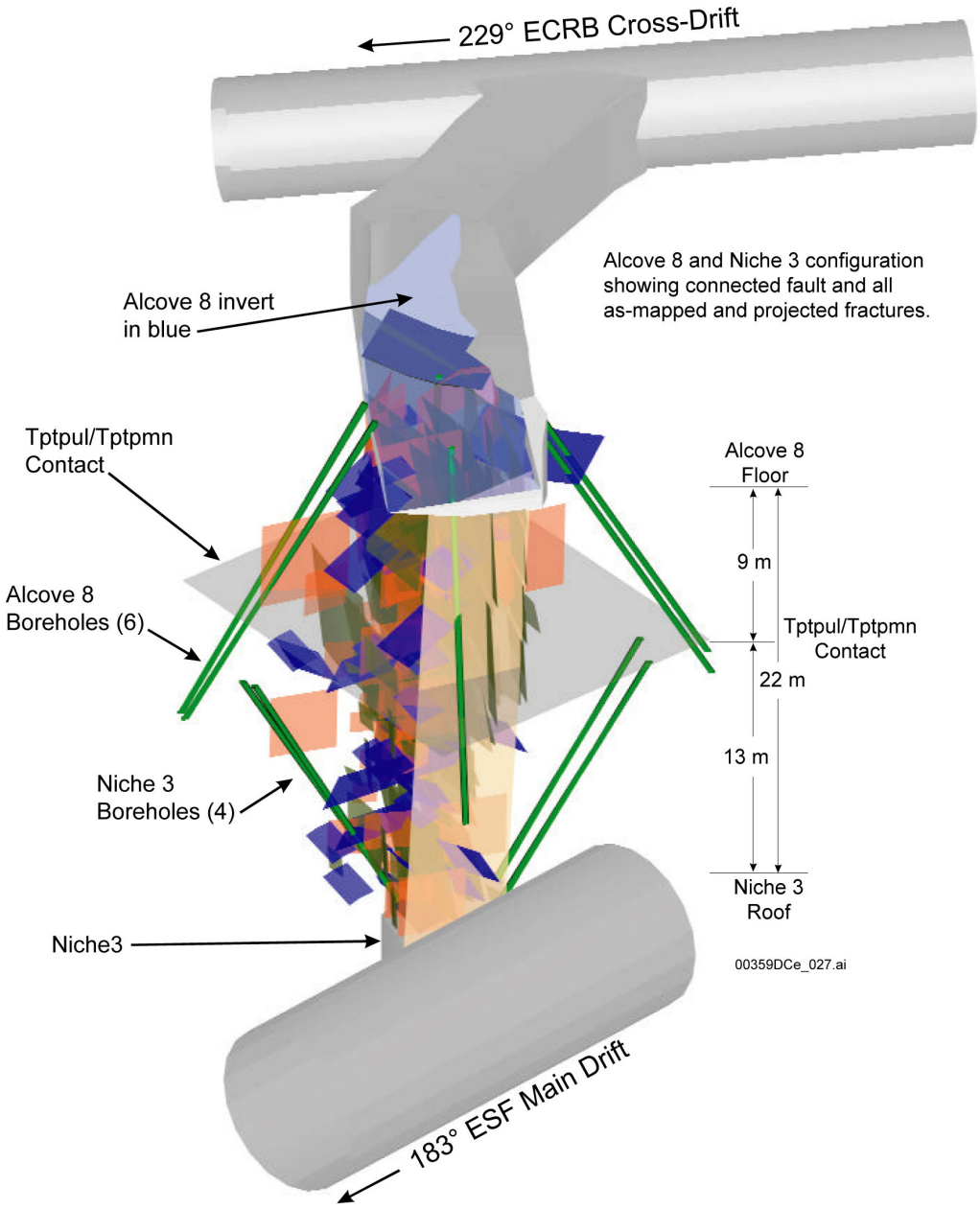

Source: Brocoum 2001a. The actual data is not in the letter, but can be obtained from a CD referenced by this letter.

Figure H-4. Three-Dimensional Fracture Network between the Floor Surface of Alcove 8 and the Ceiling of Niche 3 Generated Based on the Mapped Fractures on the Alcove Floor and Niche Ceiling

Fracture air permeability was measured along several horizontal boreholes around Niche 3 under both preexcavation and postexcavation conditions and along six vertical boreholes around Alcove 8 under postexcavation conditions (BSC 2003a). Before niche excavation, seven 9.0 m long horizontal boreholes were drilled into the rock along the niche axis. Along each borehole, air-injection tests were conducted for each packed-off interval of 0.3 m (1 ft), and air-permeability data were obtained. After excavation, the three boreholes located at approximately 0.5 m above the ceiling were left, and the others were excavated with the rock

block. In addition, seven 6.0 m long radial boreholes were drilled inside Niche 3 (see Figure H-5). Air permeability was also obtained for the three above-niche boreholes and the seven radial boreholes under postexcavation conditions. The obtained fracture permeability varied along boreholes and between different boreholes. Mean and standard deviation of log air permeability for the borehole cluster around Niche 3 were −13.4 ±0.70 under preexcavation conditions and −12.40 ±0.82 under postexcavation conditions. This indicates that the postexcavation air permeability is one order of magnitude higher than the preexcavation counterpart because of the niche-excavation-induced stress release (BSC 2003a, Table 6.1.2-5). However, the niche excavation had little effect on the pattern of air-permeability profiles along each borehole. This can also be seen from the standard deviation of similar results for both conditions. For Alcove 8, the air-permeability data obtained for the six vertical boreholes produced a mean and standard deviation −13.10 ±1.29 in terms of log permeability (BSC 2003a, Table 6.1.2-5).

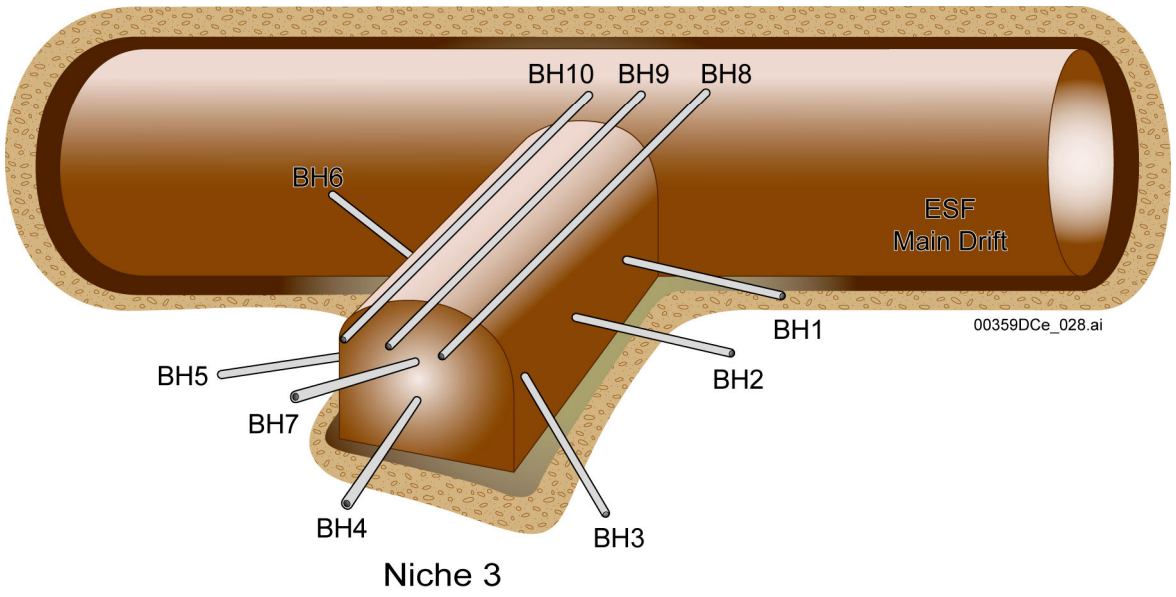

Source: BSC 2003a, Figure 6.12.1-4.

Figure H-5. Schematic Illustration of Three Horizontal Boreholes above the Niche Ceiling and Seven Radial Monitoring Boreholes Drilled in Niche 3

H.4.1.3 Experiment Setup

The large-plot infiltration-seepage test (Stage 1 of Phase I) was conducted in the Alcove 8–Niche 3 system to investigate unsaturated flow in fractured rock. The test was performed from August 20, 2002, to March 24, 2003. There were three distinct components of flow investigation: (1) controlled release of water into infiltration subplots on the alcove floor, (2) collection of seepage from the niche ceiling, and (3) borehole monitoring for changes in saturation and water potential.

The infiltration test quantified fracture permeability and percolation fluxes in the Topopah Spring welded tuffs and provided support for the analysis and validation of the unsaturated flow model. On the floor of Alcove 8, a plot of 3 by 4 m was trenched and used as an infiltration area.

The large plot was divided into 12 separated subplots, each with the same area of 1 m by 1 m (see Figure H-2). Each subplot was connected to a permeameter, through which water was applied. The volume of applied water (about 15.6 L) was calculated gravimetrically for each fill–empty cycle. The time for the refill was recorded, and then the flux was calculated for each record using the volume of applied water and the duration of the fill–empty cycle. Uniform infiltration was assumed for each fill–empty cycle. The water level in each subplot was controlled to be approximately 2 cm above the test bed. It was assumed that the rate applied to the permeameter was identical to the infiltration rate into the fractured rock, except for the first day. The first-day infiltration rate for each subplot did not include the water storage of 20 L used to establish the 2 cm water level. Occasionally, the water level in some subplots was not maintained at 2 cm because of leaks in the permeameters. When such a situation was found, the water in the subplots was removed to adjust the water level to the planned 2 cm. To reduce evaporation from the infiltration subplots, the infiltration plot was covered. Evaporation and the ventilation of the ECRB Cross-Drift had little effect on the water balance of the infiltration-seepage test (BSC 2003a).

Seepage was collected in Niche 3 by a capture system. The capture system consisted of 176 0.3 m by 0.3 m (1 ft by 1 ft) compartments used previously by Trautz and Wang (2002, Figure 2). The total cross-sectional area of the capture system was about 16.35 m^2, with some space left between compartments for maintenance. These compartments were classified into eleven tray units of different surface areas based on the field characteristics (see Figure H-3). An additional (twelfth) collection tray unit was used to collect seepage water flowing along the right wall of the niche. Initially, multiple smaller trays (i.e., units) were installed, which were subsequently grouped into larger comparable units based on observed seepage patterns. The water dripping into each of the tray units was collected into a container connected with this unit. Each container was connected to a pressure transducer to remotely monitor seepage rate and volume. Using this system, the seepage rates (in liters per day) were recorded for the container related to each collection tray unit. The seepage rates in different tray units were used to investigate the spatial variability in the seepage from the niche ceiling, as discussed in Section H.4.2.2.2. To minimize the effects of evaporation resulting from ESF main drift ventilation, the bulkhead door at the entrance to the niche was closed and sealed. The measured humidity ranged from 90% to 100% during the test period, implying that evaporation had little effect on water mass balance.

Within the fractured rock, changes in saturation (and water potential) were monitored using boreholes drilled around Niche 3. For each borehole, the electrical resistivity probes located at 0.25 m intervals along the borehole length recorded the electrical resistivity of fracture water during the entire field investigation. A sharp drop in the electrical resistivity monitored indicated an increase in fracture saturation, which was, in turn, representative of the arrival of the wetting front of liquid flow within a fracture network (Salve et al. 2003). These monitoring boreholes included three horizontal boreholes located above the niche ceiling and seven radial boreholes drilled inside the niche.

H.4.2 Fracture-Informed Analysis of Test Results

The infiltration subplots and seepage tray units were used to investigate the spatial and temporal variabilities in infiltration and seepage rates. The spatial and temporal variabilities of measured

infiltration rates and seepage rates were then analyzed in detail. A positive correlation between the infiltration rates and the fracture density on the alcove floor was obtained, but no correlation was obtained between the seepage rates and the fracture density on the ceiling of Niche 3.

H.4.2.1 Infiltration Results and Analysis

H.4.2.1.1 Temporal Variability in Total Infiltration Rate

Three stages of infiltration can be identified in the time series of daily infiltration rate through the entire large plot, as shown in Figure H-6. The total infiltration rate at a given time is defined by the overall infiltration rate through the entire large plot. On the first day, infiltration rate reached a value of 644 L/day. The total infiltration rate decreased sharply in the following five days (the first stage) and reached 61 L/day at the fifth day. In the second stage, the infiltration rate increased steadily to a value of 334 L/day after 29 days. Once the infiltration rate reached this peak value, the infiltration rate decreased in the third stage (from the 29th day to the 215th day). In the third stage, the infiltration rate decreased sharply within the first 40 days, at the end of which the infiltration rate was 64 L/day. This rate remained relatively stable until the 120th day, when the infiltration rate decreased further to approximately 50 L/day, after which it continued to gradually decline. The maximum infiltration rate on the first day was about 13 times as large as that under the quasi-stable conditions after 120 days of liquid release (BSC 2003a, Section 6.12.4).

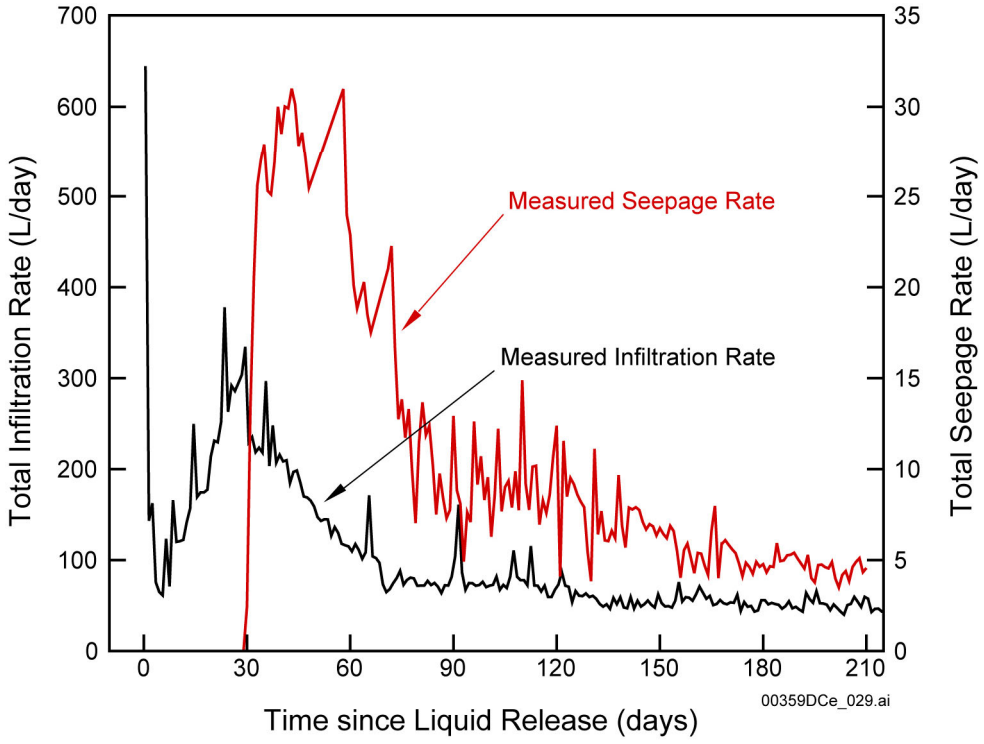

Source: DTN: LB0312A8N3MDLG.001.

Figure H-6. Total Infiltration Rate Measured through the Large Infiltration Plot and Total Seepage Rate Collected through the Ceiling of Niche 3

Around the main trend of the three-stage infiltration series, there were high-frequency fluctuations during the entire infiltration period. These infiltration dynamics may be caused by the dynamic movement of the particles of in-fill materials within fractures, the dynamic connectivity of water-conducting fractures, and the instability of entrapped air within the fracture network.

The high infiltration rate observed in the first day of liquid release was caused by water storage within initially relatively dry fractures and cavities within the layer immediately beneath the large plot. During the first day, the infiltrated water flowed quickly into connected fractures and cavities within the layer and was imbibed into the unsaturated matrix. The large estimated fracture porosity within the upper unit (6.6% for both fractures and cavities) led to the large capacity of the fractures and cavities to store water (BSC 2003a). For example, the total amount of infiltrated water in the first day could be stored within the void space of the 0.9 m thick layer of fractured rock. When the capillary imbibition into the matrix was considered, a thinner layer of the fractured rock was involved in the first-day high infiltration rate. Within the layer with ponding condition at its top, the fractured rock may be fully saturated (or highly saturated) and the liquid phase may be pervasive, as discovered in many laboratory and field tests (Su et al. 1999; Glass et al. 2002).

Figure H-7 shows the fitted Horton infiltration equation using the measured total infiltration rates (Faybishenko et al. 2003). The Horton infiltration equation can be written as:

$$I(t) = I_{\min} + \left(I_{\max} - I_{\min}\right)\exp\left(-\beta t\right) \qquad \text{(Eq. H-1)}$$

where $I(t)$ is the infiltration rate at time t, $I_{\max}$ and $I_{\min}$ are the maximum and minimum infiltration rates, and β is the decay parameter. The curve fitting was performed using the nonlinear least square fitter with a first order exponential decay function. In this curve fitting, the daily infiltration data from the 2nd to the 29th day were excluded before the infiltration peak occurred, because the main trend of total infiltration rates was disturbed by many affecting factors. The good match indicates that the temporal trend of measured total infiltration rate can be captured by the Horton equation. The Horton equation was developed for infiltration through soils and porous media to describe the reduction of infiltration rate caused by exhaustion processes, including surface and fracture ceiling, redistribution of particles, and entrapped air.

In fractured rock, the reduction in infiltration rate may result primarily from the failure of water-conducting fractures (and active portions of fractures) to transfer water (Faybishenko et al. 2003). The internal fracture connectivity is complicated: some fractures may not connect with other fractures, while others are connected to each other; only a small fraction of all fractures are globally connected. Fracture connectivity is also related to the scale of water percolation. Infiltrated water through the large infiltration plot flowed downward along fractures. Once the dead ends of fractures were reached, the infiltrated water filled in the dead-end fractures, and these fractures no longer contributed to total infiltration. This situation is referred to as a failure of the fractures in conducting infiltrated water. The dead-end fractures affected the transient infiltration rates, but they did not contribute to steady-state flow at later time. The later time is defined for the last 125 days of the test, during which relatively stable infiltration and seepage rates were obtained. The failure of water-conducting fractures was time-dependent. As the infiltration process proceeded, more initially conducting-water fractures no longer conducted

water because they are not globally connected fractures, leading to fewer fractures conducting water flow. Therefore, the trend to decrease in the total infiltration rate can be interpreted using the internal fracture connectivity. On the first day, almost all fractures connected to the infiltration plot contributed to the total infiltration rate, leading to a high infiltration rate. As infiltration proceeded, the infiltrated water moved downward, and fracture connectivity became more important to the unsaturated flow and to the total infiltration series. As infiltrated water moved downward, fewer fractures connected to the infiltration plot contributed to the total infiltration, leading to a decrease in the total infiltration rate. At later steady-state time, the infiltrated water flowed through active globally connected fractures, and the total infiltration rate tended to be stable.

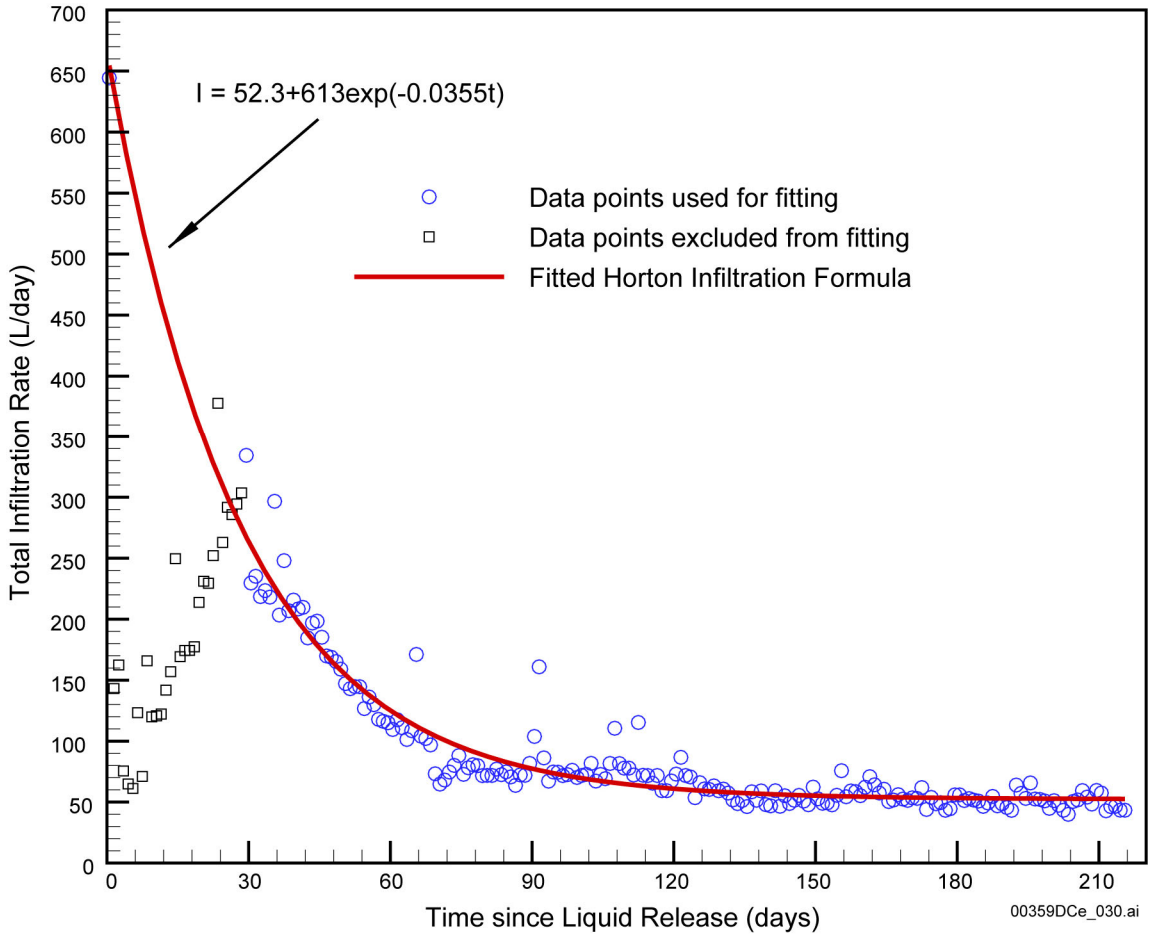

Source: DTN: LB0312A8N3MDLG.001.

NOTE: See Equation H-1.

Figure H-7. Fitting the Total Measured Infiltration Rate by the Horton Equation

The main trend of total infiltration rates was disturbed by many other affecting factors, leading to the disparity between the measured infiltration rates and the fitted ones in the first two infiltration stages. These factors included the dynamic movement (or redistribution) of particles of the in-fill materials within fractures, and the discharge and dissolution of entrapped air. In the first stage, the decrease in the infiltration rate, which was much faster than the fitted trend, may

result from the blockage of water-conducting fractures by in-fill materials. The particles on the surface of the infiltration pond and in the upper layer may migrate downward with water flow and may block flow paths by accumulating at some depth, blocking some fractures. The entrapped air may also contribute to the disparity of measured infiltration rates. Infiltrated water was imbibed by the unsaturated matrix. In the matrix within the upper unit, the ambient water saturation was 0.72 (Flint 1998), and the matrix porosity is 0.15 (BSC 2003c, Table 7). Large amounts of water can be imbibed into the matrix. As water imbibed into an initially unsaturated matrix, it pushed air out from the matrix into the fractures, thus blocking the large fractures by the entrapped air. In the second stage, the infiltration increased steadily because of the reopening of fractures blocked by in-fill materials and dissolution of entrapped air. Unlike the failure of water-conducting fractures caused by fracture connectivity, the particles blocking fractures may redistribute, leading to reopening of the previous blockage. In addition, the entrapped air can be dissolved in the flowing liquid phase, leading to reopening of blocked fractures.

H.4.2.1.2 Spatial Variability of Infiltration

Figure H-8 shows the spatial variability of infiltration in terms of the magnitude and transient pattern of infiltration rate through different subplots. Three different transient patterns of infiltration can be classified. First, the transient infiltration rate exhibited three-stage behavior as discussed for the total infiltration rate. The infiltration rate in Subplot 2 was high at both early and later time because infiltrated water may flow within a well-connected fracture network, and at later time, there were still some active fractures conducting water. The early time is defined for the first 90 days, during which infiltration and seepage exhibited strong temporal variations. For Subplots 1, 10, and 11, the infiltration rate was high in the first 90 days, but the stable infiltration rate was relatively low. This may be because of the dynamic features of the unsaturated flow and the dynamic switch or failure of water-conducting fractures. At later time, few active flow paths continued conducting water. The second infiltration pattern exhibited stable but considerable infiltration rates through the entire infiltration test. For example, the infiltration rate through Subplots 9 and 12 was relatively high, in particular at later time. This stable but considerable infiltration may be caused by some globally connected fractures beneath these subplots. These well-connected fractures were stable in conducting water. Within these well-connected fractures, the in-fill materials and entrapped air may have little effect on the stable infiltration rates. The remaining subplots (i.e., Subplots 3 to 8) had a relatively stable but low infiltration rate. For Subplots 4, 6, and 8, this may be because there are no large fractures in these subplots on the alcove floor, and the infiltrated water flowed through small fractures. The infiltration rate mainly depends on the saturated hydraulic conductivity in the saturated layer beneath these subplots, where only small fractures exist.

For Subplots 3, 5, and 8, infiltration rates are also low. Although there are large fractures intersecting these subplots, these fractures may not be globally connected, leading to low infiltration rates.

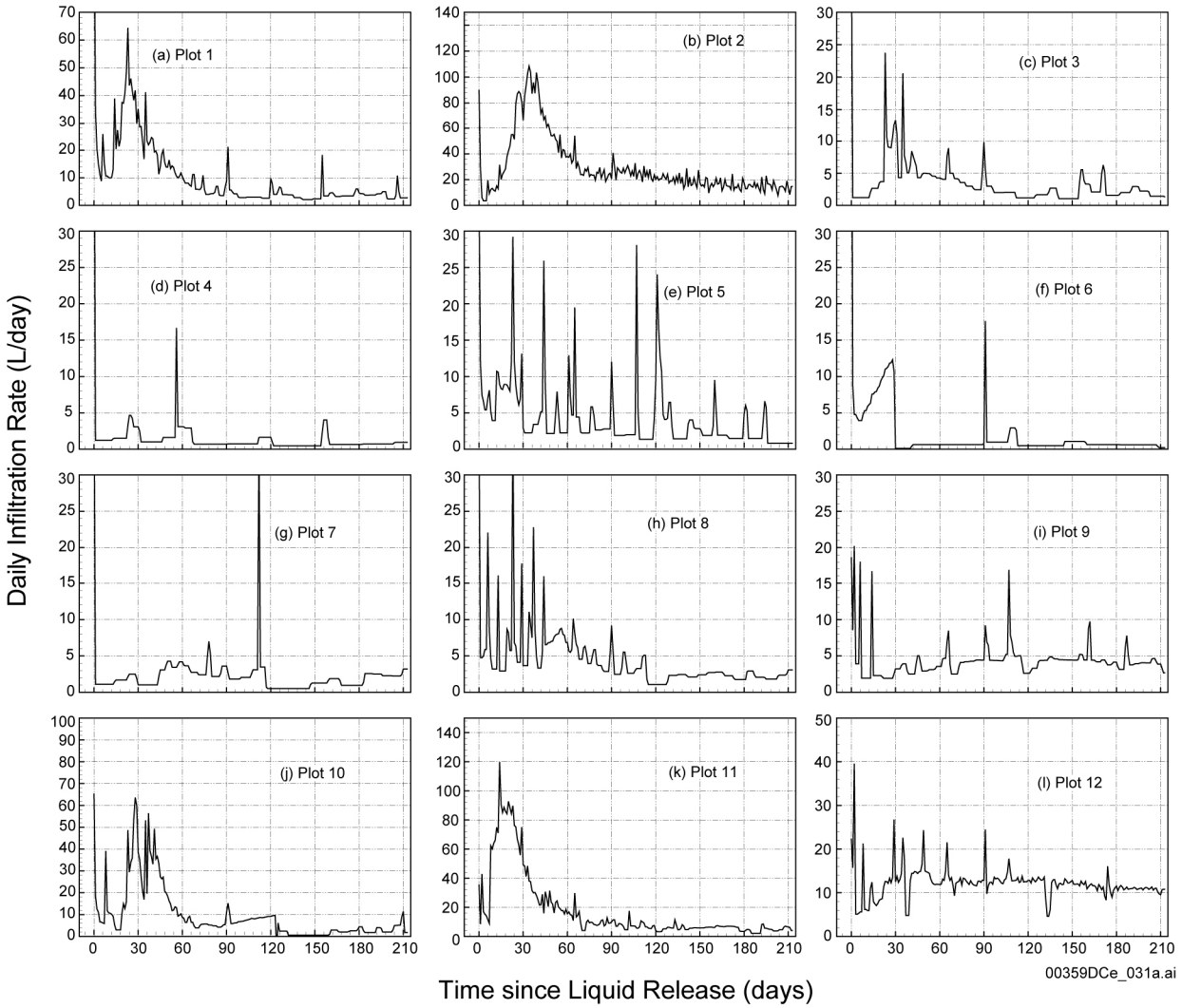

Source: DTN: LB0312A8N3MDLG.001.

NOTE: The data presented in this figure are the same as Figure 6.12.4-2 (BSC 2003a).

Figure H-8. Transient Series of Daily Infiltration Rates Measured at 12 Infiltration Subplots Located on the Floor of Alcove 8

Figure H-9 and Table H-2 shows the normalized infiltration rates through each subplot in the first 90 days and in the later 125 days. The normalized infiltration rate of a subplot at early (or later) time was calculated by dividing the mean infiltration rate for the subplot averaged for the early (or later) time by the mean total infiltration rate for the same time period. At early time (the first 90 days), the averaged total infiltration rate was 158 L/day. Subplot 2 was the most permeable subplot for infiltration, accounting for 28% of the total infiltration rate. Subplots 1, 10, and 11 were also very permeable, contributing 44% to the total infiltration rate. Subplots 4, 6, and 7 were the least permeable, and the sum of their average infiltration was just 5% of the total infiltration rate. At later time, the infiltration rate was relatively stable, and the average daily total infiltration rate was 60.5 L/day. Subplots 3 through 8, the least permeable subplots with the lowest infiltration rates, shared the same contributing percentage as at early time. However, a significant change in contributing percentage occurred in the other permeable

subplots. Subplot 12 accounted for more total infiltration rate, increasing from 8% at early time to 20% at later time. Subplots 1, 10, and 11 produced much less infiltration (23%) at later time than at early time (44%). Contribution from Subplot 2 to the total infiltration rate increased slightly to 31%.

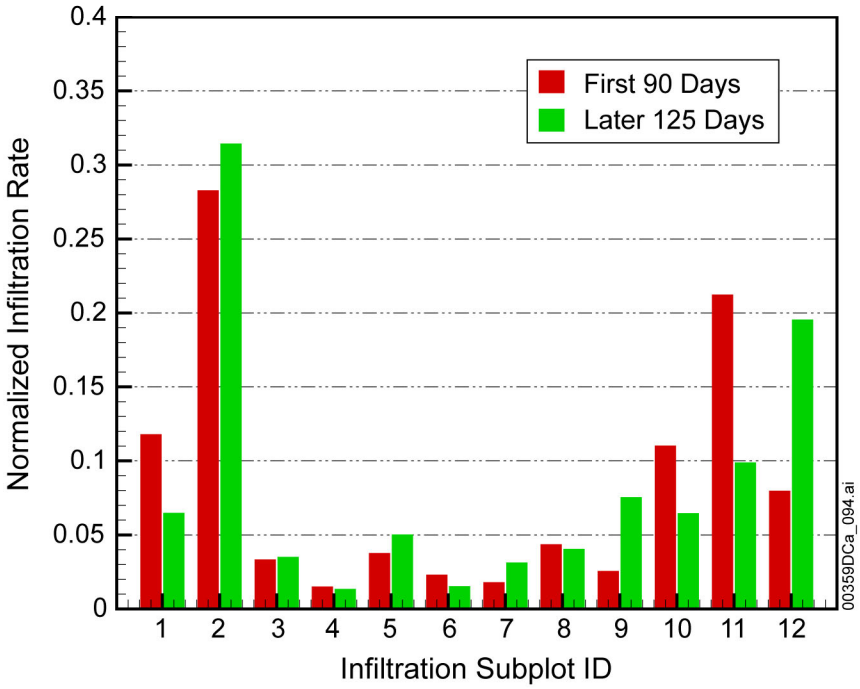

NOTE: The normalized infiltration rates are calculated using the data set in DTN: LB0312A8N3MDLG.001.

Figure H-9. Spatial Variability of (Normalized) Measured Infiltration Rates Averaged in the First 90 Days and in the Later 125 Days

Table H-2. Calculation of Normalized Infiltration Rates for the 12 Infiltration Subplots

Subplot Number	First 90 days		Later 125 Days	
	Average Infiltration Rate (L/day)	Normalized Infiltration Rate	Average Infiltration Rate (L/day)	Normalized Infiltration Rate
1	18.6722	0.1180	3.9239	0.0648
2	44.7567	0.2828	19.0253	0.3144
3	5.2843	0.0333	2.1291	0.0351
4	2.3895	0.0151	0.8137	0.0134
5	5.9668	0.0377	3.0410	0.0502
6	3.6534	0.0230	0.9239	0.0152
7	2.8511	0.0180	1.8985	0.0313
8	6.9046	0.0436	2.4549	0.0405
9	4.0458	0.0255	4.5661	0.0754
10	17.4718	0.1104	3.9101	0.0646
11	33.6111	0.2124	5.9891	0.0989
12	12.6304	0.07982	11.8298	0.1955

Source: DTN: LB0312A8N3MDLG.001.

H.4.2.1.3 Correlation between Infiltration Rate and Fracture Density

Figure H-10 shows positive correlations between normalized infiltration rates (in the first 90 days of high infiltration and in the later 125 days of quasi-stable low infiltration) and fracture density. The fracture density for a subplot was calculated by dividing total fracture trace length surveyed over the surface area of the subplot by the surface area (1 m by 1 m) (Bear et al. 1993). The fracture trace length was measured by hand on the fracture map on the alcove floor (Table H-3). A number of large fractures intersect the large infiltration plot, allowing for infiltration through the fractures (see Figure H-2). Fracture density varies from zero in some subplots to 3.92 per meter in Subplot 11, with an average value of 1.2 per meter for the large plot. Four different cases for the relation between measured infiltration and fracture density may be classified for the 12 subplots.

In the first case, when fracture density is zero (no large fractures longer than 1.0 m are involved), infiltration rate is generally low (e.g., for Subplots 4, 6, and 8). The low infiltration rate occurs through small fractures, not included in fracture maps. In this case, infiltration rate was relatively stable since the first-day high infiltration, which depended on the water-storage capacity of small fractures and cavities and the imbibition of unsaturated matrix. Beneath these infiltration subplots, the global connectivity of fractures may be weak, leading to low infiltration after the first day. The infiltration rate mainly depends on the saturated hydraulic conductivity in the saturated layer beneath these subplots.

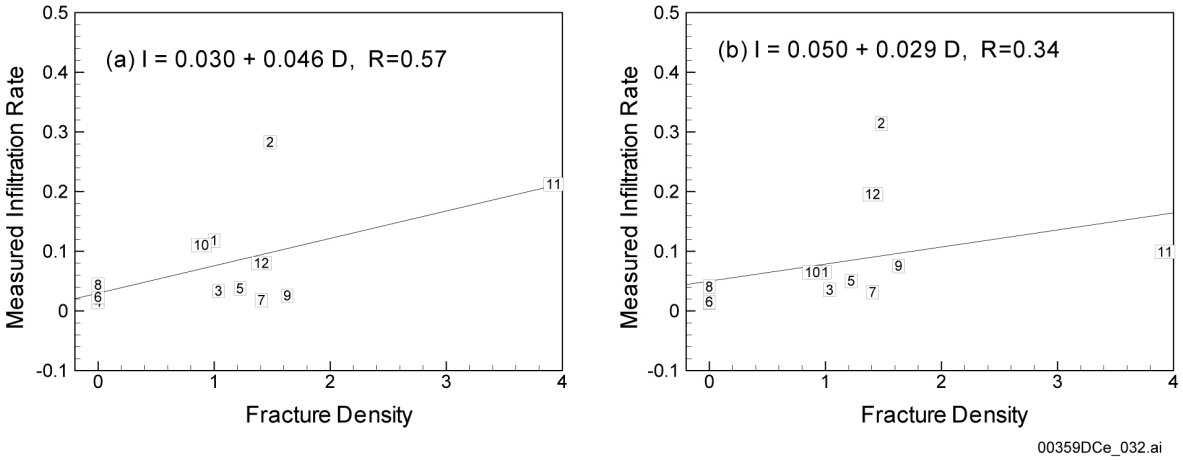

Source: DTN: GS030108314224.001 (for calculating fracture density), LB0312A8N3MDLG.001 (for calculating normalized infiltration rates).

NOTE: R is the correlation coefficient.

Figure H-10. Correlation between the (Normalized) Measured Infiltration Rates during (a) the First 90 Days and (b) the Later 125 Days, and Fractures Density Calculated for Each of the Subplots at the Floor of Alcove 8

Table H-3. Calculation of Fracture Density on the Alcove Floor

Subplot Number	Fracture Density (per meter)
1	1.00
2	1.48
3	1.04
4	0.00
5	1.22
6	0.00
7	1.41
8	0.00
9	1.63
10	0.89
11	3.93
12	1.41

In the second case, one large fracture intersects Subplots 3, 5 and 7, leading to a fracture density of about one per square meter, while the measured infiltration rate is relatively low and stable with time. The low but stable infiltration rate, similar to that in the first case, imply that the mapped fractures (or fracture segments) within these subplots may not be globally connected, or may not actively conduct water flow.

In the third case, the measured infiltration rates in Subplots 1, 2, 10, and 11 are relatively high, and their fracture density is generally large. For example, four large fractures intersect Subplot 11, leading to the highest fracture density in this subplot. One or two large fractures pass through the other three subplots, leading to fracture density close to the mean value. However, these fractures in the three subplots extend out of the large infiltration plot, and the fracture trace length out of the large plot may also contribute to the measured infiltration rate because of the in-fracture-plane flow diversion (Dahan et al. 1999). The four subplots also share the similar transient three-stage pattern of infiltration series, similar to that of the total infiltration rate (see Figure H-6). The infiltration rate in Subplot 2 is high at both early and later time because infiltrated water flows within a well-connected fracture network. For Subplots 1, 10, and 11, the infiltration rate was high in the early 90 days but low in the later 125 days because of the dynamic features of the unsaturated flow and the dynamic switch or failure of water-conducting fractures at later time.

In the fourth case, fracture density in Subplots 9 and 12 is relatively large because fractures intersect the subplots. During fracture mapping it was noted that there are a large number of small fractures around these two subplots, not included in the fracture map. The mapped large fractures and the small fractures indicate that the fracture connectivity in the fractured rock under these two subplots may be strong. The strong connectivity produced a stable infiltration rate over the entire test period, with little dynamic behavior caused by redistribution of in-fill materials and discharge and dissolution of entrapped air.

Different correlation functions were obtained for the early time of high infiltration and the later time of low infiltration. The mean infiltration rate is more sensitive to the calculated fracture

density at early time than later time, as indicated by the slope parameter obtained by linear regression (see Figure H-10). The correlation coefficient is 0.57 for the early time infiltration and 0.34 for the later-time infiltration, indicating that correlation between measured infiltration rate and fracture density is weaker during the later low-infiltration period than that in the early high-infiltration period. The different correlations may be interpreted using different transient behavior of infiltration processes in different subplots shown in Figure H-8. At early time, the mean total infiltration was high, indicating that more fractures and fracture portions were involved in conducting water and that fracture flow rate depended primarily on fracture density. At later time, a low mean infiltration indicated (1) fewer fractures were active in conducting water, and (2) more fragmented and focused flow occurred within individual fractures due to in-plane heterogeneity. The active fractures (or fracture portions) are more important to the stable infiltration rate than the fracture density, which includes both active and inactive fractures and fracture portions within individual fractures.

The positive correlations between measured infiltration rates and fracture density demonstrate that discrete fractures in the large infiltration plot play a critical role in water percolation. However, the measured infiltration rates reflect the effects from the total actively participating fractures and fracture portions, while the fracture density calculated using the fracture map on the alcove floor does not distinguish active fracture segments from inactive ones. In addition, in-fracture-plane heterogeneity and complicated dynamic effects weaken such correlations, indicating that capturing the discrete features of a fracture network does not mean fully capturing the complicated unsaturated flow.

H.4.2.2 Seepage Results and Analysis

Seepage dripping from the ceiling of Niche 3 was collected using 12 tray units. Strong spatial and temporal variability in seepage rates was analyzed, and measured seepage rates and fracture density mapped on the niche ceiling was found not to correlate. Recoverability was obtained by dividing the total seepage rate measured by the capture system by total infiltration rate through the large plot. During the later stable period, the recoverability was 10%; the other 90% of the infiltrated water bypassed the niche.

H.4.2.2.1 Temporal Variability of Total Seepage Rate

The total seepage rate measured for the 12 tray units is shown in Figure H-6. Strong temporal variability in the total seepage rate exists, resulting from the temporal variability in total infiltration rate, the transient water storage in the fractured rock system, and the lateral diversion of water in a layer above the niche ceiling caused by capillarity. Seepage occurred after 30 days from when the infiltration started; then, the total seepage rate increased rapidly up to 30 L/day within 2 to 3 days. The high seepage rate remained relatively stable for about 30 days. After that, the total seepage rate declined significantly within the next 30 days (up to the 90th day after infiltration began). The total seepage rate decreased further after the 90th day, but the rate of decline was less than that in the period between 60 and 90 days.

As shown in Figure H-6, the total seepage rate declined faster than the infiltration rate after the 60th day, when the seepage rate started to decrease. About 15% of the infiltrated water seeped out of the fractured rock into the niche at early time (the first 90 days after infiltration began). At

later time (the later 125 days), recoverability was 10%. In the last 10 days, the recoverability dropped further to 8.6%. In addition, the frequency of fluctuations in the total seepage rate was higher than that in the total infiltration rate.

The transport time of wetting fronts measured along the three horizontal boreholes 0.5 m above the niche ceiling was fairly uniform for the entire ceiling. The transport time from the infiltration large plot to the borehole sensors was about 29 days (DTN: LB0308A8N3TRTM.001).

H.4.2.2.2 Spatial Variability of Seepage Rate

Figure H-11 shows the transient series of seepage rates measured through the 12 tray units at the niche ceiling. The seepage rate used hereafter is the one per subtray (0.3 by 1.2 m, or 1 by 4 ft) per day and was obtained by dividing the collected seepage rate for each tray unit by the total number of subtrays in this unit. The number of subtrays in the 12 tray units in the order from 1 to 12 is 3, 4, 4, 4, 2, 4, 2, 4, 4, 2, 8, and 2, respectively. Two different transient patterns of the seepage rate can be identified. In the first category, considerable seepage was collected during the early time period between the 30th and the 90th day. The considerable seepage resulted from the high infiltration rate during the first 60 days (or the first 90 days) and the development of water-conducting flow paths. At later time, however, the seepage rate was low and seepage occurred intermittently. Tray Units 1, 7, and 8 on the left side of Niche 3 belong to the first category. For example, a more than 1.0 L/day seepage rate was recorded through Tray Unit 7 at about the 30th day, but seepage declined quickly, and after 90 days, the seepage rate was low with intermittent fluctuations. The low, intermittent seepage at later time is related to the low total infiltration rate (about 60 L/day) at later time. First, once the flow paths were developed, the seepage at the bottom of the flow paths mainly depended on the infiltration into the flow paths; low infiltration rates led to low fracture flow (or saturation); the low fracture flow can produce much more complicated dynamic behavior in the unsaturated flow, such as fragmented and intricate liquid-phase structures (Glass et al. 2002). Second, the flow paths developed during the high infiltration period may become inactive in conducting water at later time because of internal fracture connectivity and the dynamic switch of flow paths caused by the in-fill-material particles in fractures. Finally, water diversion and capillarity around Niche 3 may prevent seepage dripping into the niche when infiltration is small. The observed low seepage rates are consistent with the findings in a series of seepage tests conducted in Niche 3 (BSC 2003a; Finsterle et al. 2003). The seepage tests were performed by pumping water into selected test intervals in three boreholes located above the ceiling. The niche seepage threshold was obtained as the largest flux of water that can be introduced into the test borehole without resulting in seepage into the niche.

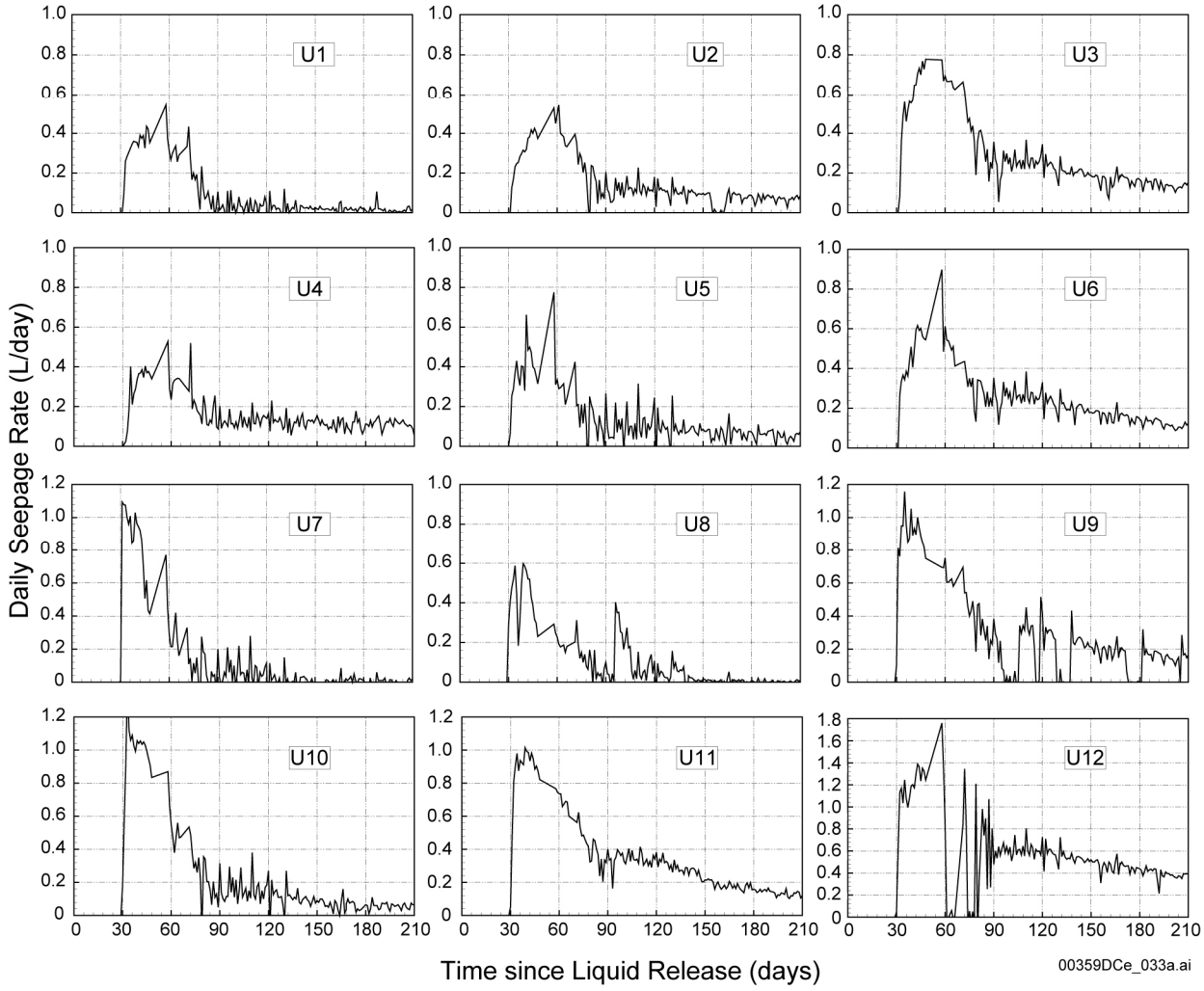

Source: DTN: LB0312A8N3MDLG.001.

Figure H-11. Transient Series of Daily Seepage Rates, per Unit Area of a Subtray, Collected for the 12 Tray Units at the Ceiling of Niche 3

In the second category, significant seepage was collected at early time, with lower but substantial flow rates measured at later time. There is a stable or quasi-stable seepage rate at later time (e.g., the seepage rate is about 0.2 L/day at the 150th day for Tray Unit 11). The maximum seepage rate of 0.5 L/day at the 150th day occurred in Tray Unit 12, which is located on the right-side wall of Niche 3. The decrease in seepage rate with time resulted from the decrease in the infiltration rate. The seepage rate at later time in these tray units may be related to stable water-conducting flow paths developing in the high-infiltration period. At early time, a number of water-conducting flow paths were developed under the high–infiltration-rate conditions, resulting in high seepage rates. With lower infiltration rates at later time, some flow paths that developed at early time may be inactive in conducting water, while the remaining flow paths may remain active in conducting water at a lower flow rate. The seepage at later time dripped into the niche from these still-active flow paths, but the flow rate and water saturation in these flow paths may be smaller.

Figure H-12 and Table H-4 shows the spatial variability of normalized seepage rates for the 12 tray units in the first 90 days and in the later 125 days. The normalized seepage rate was obtained by dividing the mean seepage rate (per unit area of a subtray) at early (or later) time by the highest mean seepage rate (in Tray Unit 12) during the same time period. The highest seepage rate per unit area occurred in Tray Unit 12, located on the right-side wall of Niche 3. Tray Unit 11 produced the second highest seepage rate at both early and later time. It was also the biggest contributor to the total seepage rate because this unit is of eight subtrays and a high seepage rate at both early and later time. The lowest seepage rate occurred in Tray Unit 1 at both early and later time. The spatial variability in the seepage rate is strong, and this strong variability may be correlated to fracture patterns on the niche ceiling.

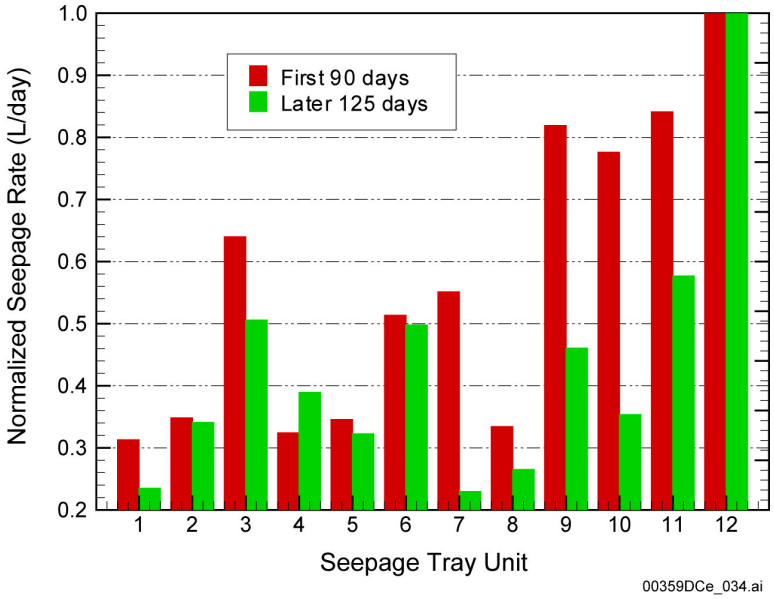

Source: DTN: LB0312A8N3MDLG.001 for calculating normalized seepage rates.

Figure H-12. Spatial Variability of Normalized Seepage Rates (per Subtray) Averaged in the First 90 Days and in the Later 125 Days

Table H-4. Normalized Seepage Rates for the 12 Seepage Tray Units

Tray Unit		Normalized Seepage Rate For the Early 90 Days	Normalized Seepage Rate For the Later 125 Days
Number	Name		
1	U4-B2	0.314	0.045
2	U4-B3	0.349	0.177
3	U4-B4	0.641	0.383
4	U3-B2	0.325	0.238
5	U3-B3	0.346	0.154
6	U3-B4	0.514	0.373
7	U4-B1	0.552	0.038
8	U1-B5	0.335	0.082
9	U1-B4	0.820	0.327
10	U1-B3	0.777	0.193
11	U1-B1	0.842	0.472
12	U3-B5	1.00	1.00

Source: DTN: LB0312A8N3MDLG.001.

H.4.2.2.3 Correlation between Seepage and Fracture Density

Figure H-13 shows the correlations between normalized seepage rates (at early high-infiltration and later low-infiltration time) and fracture density on the niche ceiling. The fracture density was calculated for each tray unit using the large natural fractures (longer than 1.0 m) on the fracture map shown in Figure H-3. The fracture density was obtained by dividing the total fracture trace length surveyed for a tray unit by its total surface area (Table H-5). No correlation was found for the early-time seepage rates, while a weakly negative correlation was found for the later-time seepage rates. The lack of correlation can be interpreted using the complexity of unsaturated flow in fractured rock under low percolation-rate conditions and the flow diversion in the vicinity of Niche 3.

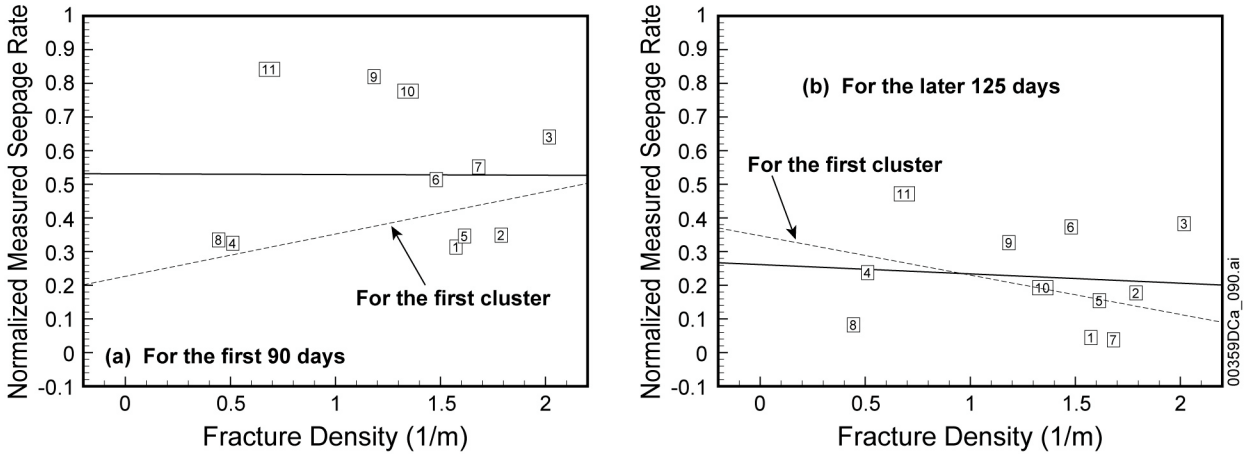

Source: DTN: LB0312A8N3MDLG.001 (for Calculating Normalized Seepage Rates), and DTN: GS030108314224.001 (for Calculating Fracture Density).

Figure H-13. Correlation between the Normalized Measured Seepage Rates and Fracture Density Calculated for Each of the Tray Units at the Ceiling of Niche 3 for the Early and Later Times, as well as Correlation for the First Flow-Path Cluster

Table H-5. Calculation of Fracture Density on the Niche Ceiling

Tray Unit Number	Fracture Trace Length (m)	Number of Subtrays	Surface Area of Tray Unit (m^2)	Fracture Density (per meter)
1	2.75	3	1.11	1.57
2	2.65	4	1.49	1.79
3	3.00	4	1.49	2.02
4	0.75	4	1.49	0.51
5	1.20	2	0.74	1.61
6	1.10	4	1.49	1.48
7	2.20	2	0.74	1.68
8	1.25	4	1.49	0.44
9	0.65	4	1.49	1.18
10	1.00	2	0.74	1.35
11	2.05	8	2.97	0.69

The variably saturated flow in the fracture network transited from fully saturated flow in the upper portion of the system to complicated unsaturated flow under low-percolation conditions in the lower portion of the system, in particular in the vicinity of the niche. First, seepage dripped into the niche through fractures because of dominant fracture flow and little matrix flow in the lower hydrogeologic unit. Second, in-fracture-plane heterogeneity led to fragmented and fingered flow within single fractures; such a flow may not be a function of fracture trace length represented by fracture density. Flow fragmentation and fingers are major features of unsaturated flow in fractured rock under low-flow-rate conditions (Glass et al. 2002). Third, the mapped fractures on the niche ceiling may be globally connected, but they may be inactive fractures, and the global unsaturated flow may occur in a fraction of connected fractures, as indicated by the active fracture model (Liu et al. 1998). The lack of correlations demonstrates the importance of active fragmented and fingering flow within single fractures and active fractures in a fracture network.

The lack of correlation between normalized seepage rate and calculated fracture density also demonstrates the importance of water diversion around the niche caused by (1) small fractures and excavation-induced fractures, (2) capillary barrier layer effect, and (3) film flow on the niche ceiling. First, small fractures and excavation-induced fractures may be connected with water-conducting fractures above the niche. For example, water in a water-conducting fracture, which ends at a distance above the ceiling, can be redistributed (or diverged) into such connected small fractures and dispersed on the niche ceiling. In addition, small fractures may imbibe water at fracture intersections from large fractures because the small fractures have higher capillarity than the large fractures, but the small fractures are not included in the fracture map on the niche ceiling and thus not considered in the correlation analysis. The excavation of the niche induced many fractures around the niche ceiling. These induced fractures enhance fracture connectivity in different directions, facilitating flow diversion. Second, capillarity is an important mechanism for water diversion around the niche ceiling (Philip 1990; Finsterle 2000). Because of the zero-capillarity condition on the ceiling and sidewall of Niche 3, a capillary-barrier layer existed above the niche ceiling. Within the capillary layer, flow can redistribute among all connected fractures, leading to less correlation between seepage rates and calculated density of large fractures. Finally, water flow leaving from fractures may flow along the niche ceiling in the

form of film flow (Tokunaga and Wan 1997). The film flow may be caused by surface roughness and the geometric shape of the niche ceiling. Film flow on the niche ceiling has been observed in seepage tests in Niche 4 (also referred to as Niche 4788) (Trautz and Wang 2002).

H.4.2.3 Potential Flow Path Clusters

Two potential flow-path clusters can be identified using the transient patterns of measured seepage rates in different trays (see Figures H-11 and H-12), and the fracture maps on the alcove floor and the niche ceiling (see Figures H-2 and H-3). Each cluster may contain a number of flow paths, which may vary with time. The measured seepage rates in the first row of trays (i.e., Tray Units 1–6) exhibited transient patterns different from those in the second row (i.e., Tray Units 7–11) in the early time between the 30th and 90th day. In the second row, the seepage rate dropped quickly after seepage occurred at approximately the 30th day. In the first row, however, seepage rate increased after the first occurrence of seepage at the 32nd day, and the seepage rate reached its peak at the 60th day. In each row, the measured seepage rates shared similar transient patterns among different trays. The seepage features (which are similar in the row, but different between the two rows) may imply that two flow-path clusters exist for the unsaturated flow. In addition, the normalized seepage rates in the two rows of trays also exhibited different behavior at early and later time, as shown in Figure H-12. Normalized-seepage-rate distribution in the first row is similar for both early and later times. However, such a distribution for the second row changes dramatically from early time to later time.

The two flow-path clusters can also be identified using the fracture maps on the niche ceiling and alcove floor. Four large fractures intersect the seepage capture system and pass through both the first and second row of trays. Fracture segments intersected in the first row contribute to the first cluster, while the segments in the second row contribute to the second cluster. The difference in the seepage rates in the two clusters results primarily from the difference in infiltration on the alcove floor. Water flow in the first cluster stems from high infiltration in Subplot 2 and its neighboring subplots. The large fracture intersected by Subplot 2 may be hydraulically connected with fractures (on the niche ceiling) intersected with Tray Units 2 and 3. The second cluster may connect segments of the four fractures in the second row to large fractures in Subplot 11 and its neighbors, through which infiltrated water exhibits an earlier infiltration peak (on the 15th day) than in the first cluster.

The two flow-path clusters exhibit different correlations between the normalized seepage rates and fracture density. At early time, infiltration was high, resulting in a high flow rate and less focused flow within fractures. A positive correlation was found with a correlation coefficient of 0.49 for the first cluster. In this cluster, high seepage rate corresponds to high fracture density. For example, Tray Unit 3, intersecting three large fractures, has relatively high seepage rates, whereas Tray Unit 4 has a shorter fracture trace length and lower seepage rates. A weaker correlation (with correlation coefficient of 0.27) was obtained for the second cluster, indicating that seepage is more complex for the second cluster. Tray Unit 11 has the second highest seepage rate, while its fracture density is relatively small, indicating that the high seepage rate may focus within a short fracture trace length. At later time, no correlation was obtained between seepage rates and fracture density for either flow-path cluster, because fragmented flow and fingers may occur within single fractures. Evidence of fragmented and fingered flow can be seen in the seepage through the two fractures intersecting Tray Units 2, 3, 7, and 8. The fracture

segments in the first cluster continued to contribute to substantial seepage, while those in the second cluster carried little flow, resulting in small, intermittent seepage. However, at early time, all fracture segments of the two fractures are active in conducting seepage. This demonstrates that more fragmented and fingered flow occurs under low-flow-rate conditions, leading to a weaker correlation between seepage rates and fracture density. Under higher-infiltration conditions, the unsaturated flow is more pervasive and the correlation is higher.

H.4.3 Model Calibration Using Available Hydrogeologic Data

The measured infiltration and seepage rates in the large-plot test are representative of the unsaturated flow in the discrete fracture network and interaction with the matrix. The measured seepage rates are also representative of the lumped effects of fracture connectivity and flow within the active fracture network. To reproduce the temporal and spatial variability of infiltration and seepage measured in the large-plot test, a three-dimensional unsaturated flow model was developed, and the column-based heterogeneity was introduced. The model was calibrated using the measured infiltration series in each subplot and the seepage rate series in each tray unit.

The continuum approach was used to simulate the unsaturated flow (with strong transient behaviors) in fractured rock. This approach has been justified as applicable to the unsaturated flow at Yucca Mountain (Doughty 1999; Finsterle 2000; Finsterle et al. 2003; Liu et al. 2003). The multiple interacting continuum (MINC) approach was used to accurately simulate the transient interaction of flow between the matrix and fracture continuum (Pruess and Narasimhan 1985; Pruess et al. 1999). In this approach, fractures are represented by a fracture continuum, while the matrix is represented by a number of nonoverlapping matrix continua, starting from the fracture-matrix interface to the center of a matrix block. The thickness of a matrix subblock decreases from the central matrix to the fracture-matrix interface to capture the high gradients of transient flow along the interfaces between fractures and the matrix. An alternative approach is the discrete fracture network model, in which water flow occurs in the connected discrete fractures generated (Dverstorp and Andersson 1989; Cacas et al. 1990). The discrete fracture network model is applicable to a small-scale flow problem because the detailed characteristics of fractures are needed in the modeling. However, this model may not be applicable to the mesoscale flow system presented here because of two considerations: (1) only the fracture maps on the alcove floor and niche ceiling are available (with large fractures mapped); the fracture network of the 21 m thickness is largely unknown because of the strong variability in fracture frequency and trace length discussed above; (2) the spatial variability in measured seepage and infiltration can be deterministically obtained through model calibration using the measurement data, which constrain the model well.

H.4.3.1 Model Development

To capture the infiltration and seepage measured in the large-plot test, column-based heterogeneity was used in the modeling analysis. For each hydrogeologic unit, a number of rock columns are selected, based on available data concerning the flow system (e.g., flow rate) and measured rock properties. Uniform rock properties within each rock column are assumed, while different rock properties may exist between different rock columns. The flow redistributes among different columns within the same hydrogeologic unit because of lateral difference in

rock properties. The introduced deterministic heterogeneity was based on three considerations. First, previous fracture-network modeling has demonstrated that unsaturated flow paths within a fracture network are generally vertical as a result of gravity-dominated flow behavior (Liu et al. 2002). Second, the mapped fractures are near vertical in the study area and around the ESF main drift and ECRB Cross-Drift. Finally, available fracture data are not enough to characterize detailed flow paths between Alcove 8 and Niche 3, and a simple model of heterogeneity generally involves a relatively small number of parameters that need to be calibrated.

The number of rock columns within the upper (or lower) unit was determined based on available data (for model calibration) on the infiltration (or seepage) series. For example, 12 infiltration subplots with measured infiltration rates were available. As a result, there were 12 rock columns in the upper unit, each of which corresponded to an infiltration subplot. An additional rock column was used for the rock mass surrounding the 12 central columns. The same method was used to define the rock columns in the lower unit. Thus, there were 12 rock columns for the lower unit, each of which corresponded to the configuration of a collection tray unit. Tray Unit 11, the large tray unit, was divided into three parts and regrouped into three rock columns, ranging from 10 to 12, because the same discretization in the x direction was used in the numerical grid for a row of gridblocks in the y direction. An additional rock column for the rock mass surrounding the 12 central columns was also used. In addition, fracture maps on the alcove floor and on the niche ceiling roughly constrain the calibrated rock properties.

For each of the central rock columns, there was a measured infiltration (or seepage) series for calibrating rock properties within the column. To reduce the number of rock parameters (unknowns), only the most sensitive parameters to the measured flow rate were considered, while all other rock parameters were assumed to be uniform within a hydrogeologic unit. In this case, fracture permeability and fracture van Genuchten α were the most important rock properties for water redistribution, while fracture van Genuchten m was assumed to be homogeneous within each of the two hydrogeologic units (van Genuchten 1980). Uniform permeability and van Genuchten parameters were used for the matrix continuum for each hydrogeologic unit because the correlation scale length of matrix rock properties is large relative to the test system dimensions (Zhou et al. 2003).

As a result, there were two unknowns to be calibrated for each of the 26 rock columns. For the lower unit, the measured seepage series over 215 days may constrain the two unknowns for each rock column. However, for the upper unit, the infiltration rate into a rock column is sensitive to the saturated hydraulic conductivity in the thin saturated layer beneath the corresponding infiltration subplot, but it is not sensitive to the van Genuchten α in the rock column. To better constrain the van Genuchten α in the upper unit, a uniform α was used for the 12 central rock columns. There were, thus, 26 unknowns for the lower unit and 15 unknowns for the upper unit.

A three-dimensional numerical model was developed to simulate the variably saturated flow in fractured rock. In the model, the air phase was assumed to be passive, and only unsaturated liquid flow was simulated in order to reduce the computational burden on model calibration. The unsaturated flow was simulated using the EOS9 module of TOUGH2, a module for variably saturated flow of the liquid phase (Pruess et al. 1999).

A three-dimensional domain was selected as the flow system (see Figure H-14). The system was bounded on the top by the floor of Alcove 8 and on the bottom by the floor of Niche 3, with a thickness of about 25 m. The niche is located in the center and represented by a void space. For simplicity, the niche ceiling was approximated by a flat surface, at a distance of 3.2 m from the niche floor. The two-dimensional size in the horizontal direction was determined from the flow plume observed by the boreholes drilled around the niche. The system is 20 m wide and 10 m long along the niche axis. It was believed that the vertical side boundaries are at the ambient unsaturated flow conditions, away from the central flow system disturbed by the infiltration and seepage test. The 12 infiltration subplots and the projected outline boundary of the niche ceiling are also shown on the top of the grid. The contact between the upper and lower hydrogeologic unit is a horizontal surface, located at 14.5 m from the alcove floor (top boundary). To capture diverted water flow around the contact interface caused by difference in rock properties, small vertical discretization was used around the interface. Small vertical discretization was also used to accurately capture diverted water flow around the niche ceiling caused by capillary barrier effects (Philip 1990; Finsterle et al. 2003). In the horizontal plane, small grid size was used for the central area of infiltration and seepage. Each infiltration subplot covers 2 gridblocks by 2 gridblocks, and each tray unit covers 1 gridblock by 4 gridblocks. Coarse blocks were used for the area away from the central infiltration-seepage test. As discussed above, for each gridblock, there was one fracture block and five matrix blocks because the MINC method was used to represent the interaction between fractures and the matrix. In total, there were 67,320 blocks (for fracture and matrix) and 140,000 connections in the three-dimensional grid.

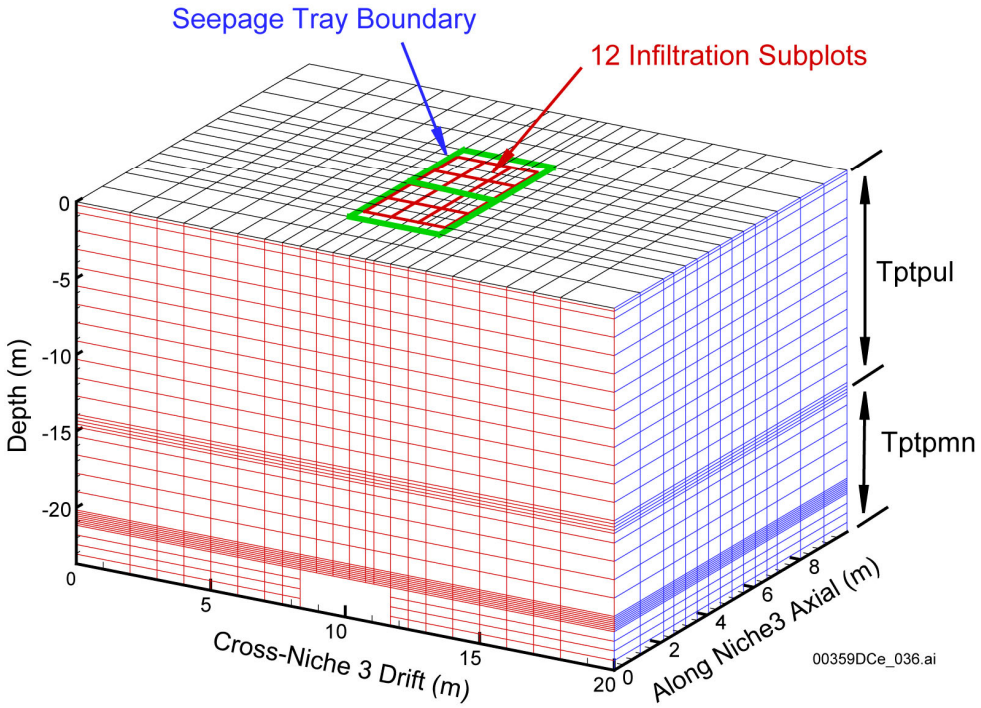

Source: DTNs: LB0312A8N3MDLG.001 and LB0312A8N3MDLG.002.

Figure H-14. Three-Dimensional Numerical Grid for the Calibration of the Large-Plot Infiltration and Seepage Tests

Two possible boundary conditions can be specified at the large infiltration plot because both water head and water flux are known from the large-plot test. The constant water pressure head (2 cm) may be specified at the infiltration plot. This condition produces stable infiltration rates over time into the underlying system because the saturated hydraulic conductivity is assumed to be time-independent, and the infiltration rate depends only on the slightly decreasing hydraulic gradient. However, the resulting infiltration series are very different from their measured counterparts, which reflect the complicated dynamic effects happening in the unsaturated system, as discussed above. Therefore, the constant-head condition is not applicable to the unsaturated flow system with strong transient behaviors. In the model calibration, the measured infiltration-rate series, reflecting the complicated dynamic behavior of the time-dependent saturated hydraulic conductivity in the layer beneath the infiltration plot, and the capacity of flow within the water-conducting fracture network, were used as boundary conditions for the large infiltration plot. The remaining area on the top boundary was assumed to be impervious. The vertical side boundary for the entire flow domain was assumed to be a no-flow one. The ceiling and side-wall boundary of the niche was modeled by a zero-capillary-pressure condition, representing capillary barrier effects. The other bottom boundary corresponded to free drainage conditions.

The initial water saturation in the matrix and fracture continua was complicated because the ambient flow condition was disturbed by a fault test conducted before the large-plot test and construction water used for excavation of the alcove (BSC 2003a). Under the ambient flow condition, matrix saturation is 0.72 for the upper unit and 0.85 for the lower unit (Flint 1998). The actual matrix saturations were expected to be higher than the ambient values because of the wetting and drying processes of the nearby fault test. In the model analysis, 0.86 and 0.92 were used as the initial matrix saturation values for the upper and lower units, respectively. A large degree of uncertainty may exist in the initial conditions used, but this uncertainty does not have a significant effect on the stable infiltration and seepage at later time of the test. Uniform fracture saturation of 1.05×10^{-2} (for ambient condition) was used for both hydrogeologic units because fractures can drain quickly and recover from previous wetting.

The rock properties of the matrix continuum used in the model are effective porosity, ϕ, permeability, k, and van Genuchten α and m. All the matrix rock properties are obtained from the calibration of rock properties for the site characterization of Yucca Mountain (BSC 2003b; BSC 2003c) because it is believed that all these rock properties are insensitive to water redistribution happening in the large-plot test. The calibrated values were obtained using available ambient flow data, rock properties, and field tests for each of the 35 hydrogeologic units of the entire Yucca Mountain site. The same four rock properties for the fracture continuum are needed in the model. The fracture van Genuchten m value is also obtained from the rock property calibration for site characterization. For fracture porosity, permeability, and van Genuchten α, however, the test-site values must be used because of the highly spatial variability in such rock properties. The test-site-specific fracture porosity for both the upper and lower units, calibrated from the fault test near the large-plot test site, was used in the model. Table H-6 show the rock properties fixed in the model calibration for the large-plot test (BSC 2003d, Table 7.6-1). The calibrated values of the remaining two rock properties (fracture permeability and van Genuchten α) by the fault test were here used as initial guesses for the model calibration of the large-plot test site.

Table H-6. Matrix and Fracture Properties Fixed in the Model Calibration for the Large-Plot Test

	Matrix Rock Properties		Fracture Rock Properties	
	Tptpul	**Tptpmn**	**Tptpul**	**Tptpmn**
Porosity	0.15	0.11	0.066	0.01
Permeability (m^2)	3.08×10^{-17}	4.07×10^{-18}	Varying	Varying
van Genuchten α (Pa^{-1})	2.13×10^{-5}	3.86×10^{-5}	Varying	Varying
van Genuchten *m*	0.30	0.29	0.61	0.61

H.4.3.2 Model Calibration

The developed flow model was calibrated to reproduce the temporal and spatial variabilities in the infiltration and seepage measured in the large-plot test. By the calibration, site-specific rock properties (and column-specific rock properties for heterogeneity) were obtained. The rock parameters to be calibrated were fracture permeability and van Genuchten α for each of the 13 rock columns in the lower unit, fracture permeability for each of the 13 rock columns in the upper unit, and van Genuchten α common for the 12 central columns and the rest of the rock mass column in the upper unit. This means that there were a total of 41 unknowns to be calibrated, 26 parameters for the lower unit and 15 parameters for the upper unit.

To reduce the number of unknowns in the upper unit, the infiltration data in 12 subplots were used to better constrain fracture permeability unknowns. For each rock column, fracture permeability was calibrated by matching the maximum measured infiltration rate (not in the first day) and the simulated infiltration rate. The maximum infiltration rate was considered to be the saturated hydraulic conductivity for the column (Faybishenko et al. 2003). The top boundary for flow in the case was the 2-cm water head, which was constant with time. The trial-and-error method was used to reduce the mismatch between the measured maximum infiltration rate and the stable infiltration rate for a given fracture permeability. The fracture permeability obtained independently for each rock column was further calibrated using a scale factor. In this way, the effects of observed spatial variability of infiltration rates were approximately captured by the model calibration, and the number of unknowns to be calibrated was reduced from 41 to 30.

As discussed above, the fracture characteristics around Niche 3 were affected by excavation-induced damage: (e.g., the fracture permeability increased by an order of magnitude after niche excavation). To account for the difference between the internal fracture rock and the rock mass in the vicinity of the niche, uniform fracture permeability and van Genuchten α were used for a thin layer (about 1.0 m) affected by the niche excavation.

In the model calibration, the measured time-dependent infiltration rates were used as the top boundary condition. The data used for the calibration included the measured seepage series for each of the 12 tray units and the transport time of 29 days in the layer 0.5 m above the niche ceiling, measured through three boreholes. Because strong temporal variability was included in the seepage rate, the entire seepage series was divided into three time periods: (1) the first 30 days, (2) the next 60 days, and (3) the next 125 days. The objective function is defined as follows:

$$obj. = \sum_{j=1}^{13} \left(\sum_{t=1}^{30} \omega_1 \left(q_{jt}^m - q_{jt}^s \right)^2 + \sum_{t=31}^{90} \omega_2 \left(q_{jt}^m - q_{jt}^s \right)^2 + \sum_{t=91}^{215} \omega_3 \left(q_{jt}^m - q_{jt}^s \right)^2 + \sum_{t=1}^{20} \omega_4 \left(0 - q_{jt}^s \right)^2 \right) \quad \text{(Eq. H-2)}$$

where q_{jt} is the seepage rate at the t day since infiltration started for the j tray unit (j = 13 is for the total seepage rate), superscripts m and s denote the measured and simulated value, respectively, and ω is the weighting factor. Different weighting-factor values were used for the different time periods. A high value of ω_3 was used to focus on the later quasi-stable time. For each tray unit, the first three terms indicate the misfit between the measured seepage rate and the simulated seepage rate, while the last term indicates the misfit between measured transport time and simulated transport time. A high weight was used for the misfit between the measured and simulated seepage rate in the first 20 days to impose constraints on the transport time. The calibration aimed to reduce the objective function by adjusting the 30 rock properties.

The calibration was performed using the inverse modeling code iTOUGH2 V5.0 (Finsterle 1999). In each forward run, the variably saturated flow in 215 days with highly transient behavior was simulated. Figure H-15 shows the match between the measured total seepage rate for the entire niche and the simulated total seepage rate using calibrated rock properties. The match is reasonable, in particular for the later time (90 days after liquid release). The good match at later time may result from a high weighting factor used for the later time seepage rate in the objective function, and the quasi-stable nature of seepage and infiltration rate. In the early time between the 30th and 90th day, the match is also reasonable. The simulated maximum seepage rate is close to the measured one. No stable stage of 30 days in the calibrated seepage series was obtained, while a stable high seepage rate of about 30 days occurred in the total measured seepage series. The stable stage in the measured seepage rate resulted from the combination of increasing seepage rate in one flow path cluster (Tray Units 1 to 6) and decreasing seepage rate in the other cluster (Tray Units 7 to 11). The simulated seepage occurs at the 20th day, earlier than the measured seepage, which occurred at the 30th day since the infiltration started. The difference in water front transport time can be explained by the handling of different kinds of data in the objective function, as discussed above.

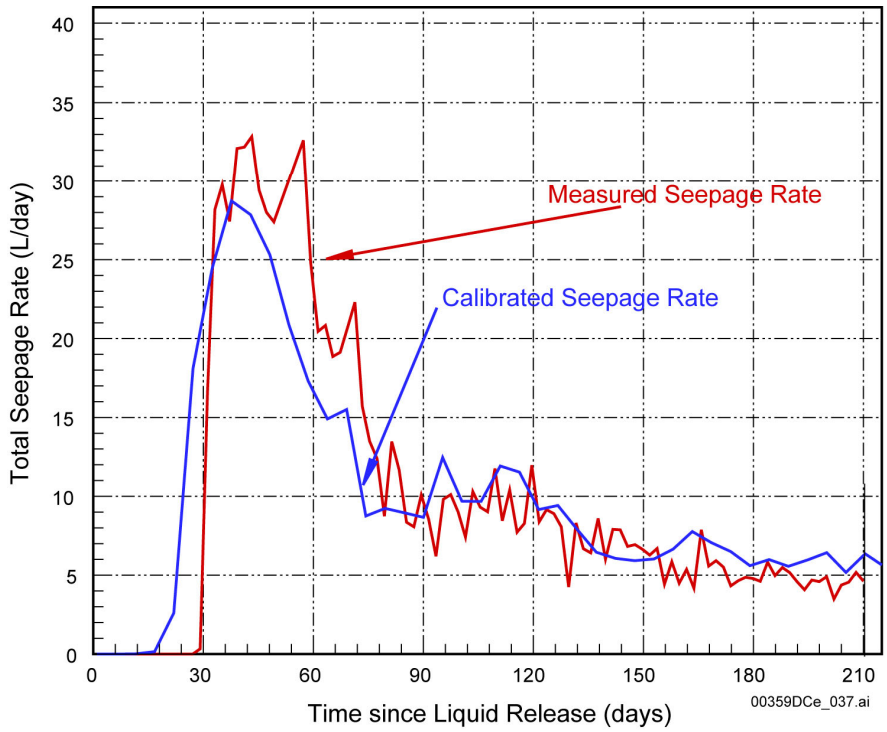

Source: DTNs: LB0312A8N3MDLG.001 (File SrunAi.tec) and LB0312A8N3MDLG.002.

Figure H-15. Match between Measured Total Seepage Rate Series and Simulated One Using the Calibrated Rock Properties

In the calibration, a large weight factor was used to keep seepage from occurring within the first 20 days, while a smaller weight factor was used for the misfit between the measured and calibrated seepage rate between 20 and 30 days, allowing for the occurrence of seepage between 20 and 30 days. The reason for this was that many retardation factors (e.g., dynamic connectivity of water-conducting fractures) affecting the wetting-front transport time cannot be considered in the numerical model. The large degree of uncertainty in initial matrix saturation values used in the model may also affect water transport time because the matrix imbibes water flowing in fractures into the matrix, delaying the water front transport time to the niche ceiling. If the first 30 days for no-seepage occurrence were used, the calibrated fracture permeability would be too small to be reasonable for the site.

Figure H-16 shows the match between the measured and calibrated seepage series associated with each of the 12 rock columns. Generally, the match is good in terms of the time-dependent seepage series. For example, the simulated and measured seepage rates for Column 12 are close to each other. For Column 7, however, there is no seepage in the simulated results, while the measured seepage occurred in the time period between the 30th and 90th day with a low seepage rate afterward. This may be caused by the high weighting factor used for the later time and the strong dynamic features in the measured seepage. For some columns, the simulated seepage declines with time less than the measured seepage at later time because of the many dynamic effects of fragmented unsaturated flow in fractured rock. The generally good match demonstrates that the calibrated heterogeneity in fracture capillary strength and permeability can be used to reproduce the spatial variability in the measured seepage rate.

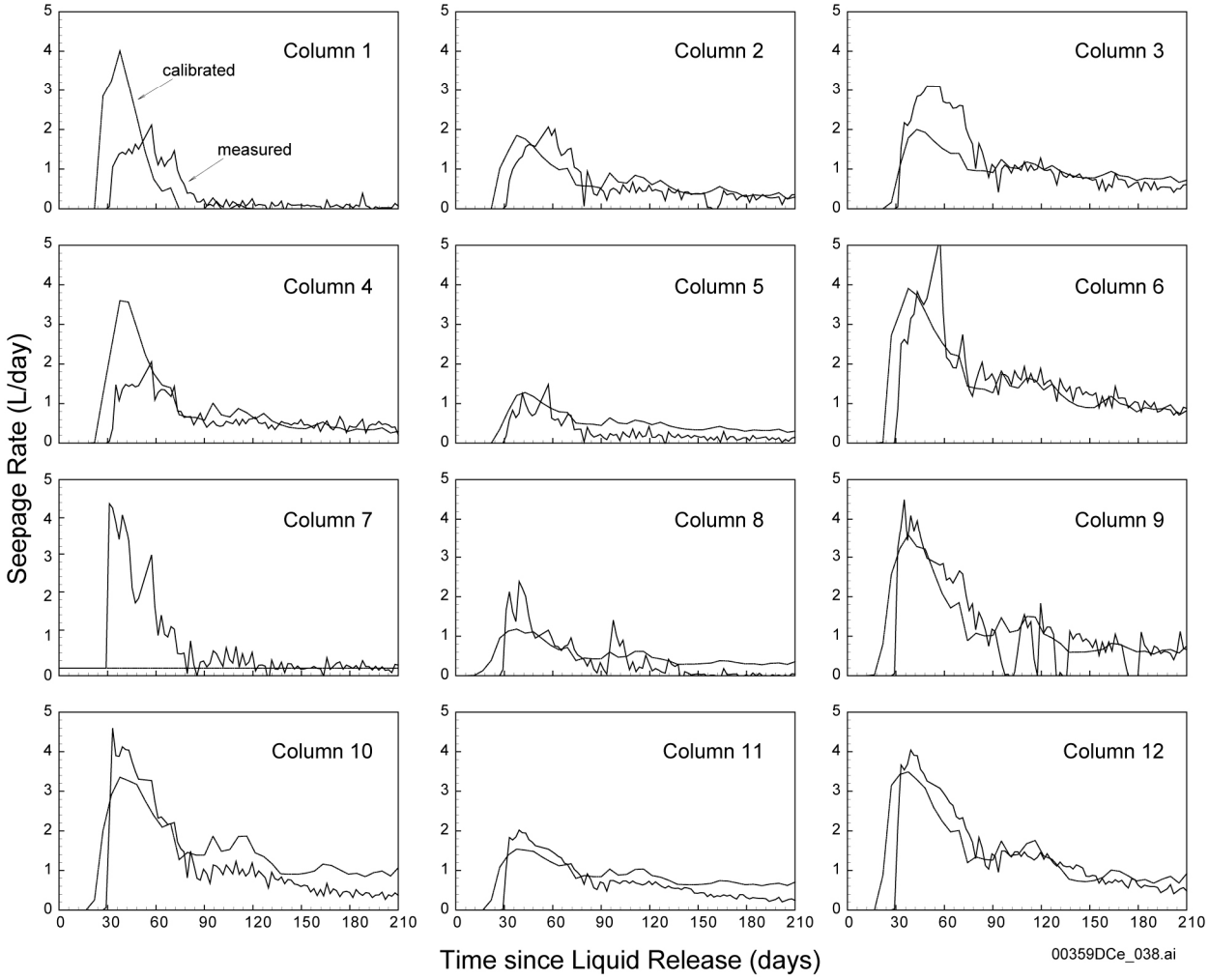

Source: DTNs: LB0312A8N3MDLG.001 (File SrunAi.tec) and LB0312A8N3MDLG.002.

Figure H-16. Match between Measured Seepage Rate Series and Simulated Ones, Using the Calibrated Rock Properties for the 12 Seepage Columns

H.4.3.3 Results and Discussion

Figure H-17 shows the calibrated fracture permeability and van Genuchten α for the upper and lower 13 rock columns. The calibration of fracture permeability in the upper unit was constrained by the maximum measured infiltration rate for each subplot associated with a rock column. The calibrated fracture permeability reflects the spatial variability in measured infiltration rate over the large infiltration plot. Calibrated fracture permeability varies over one order of magnitude in the central large infiltration plot. The largest fracture permeability of 1.86×10^{-13} m^2 is located in Column 11 (beneath Subplot 11), where the measured maximum infiltration rate is 119.7 L/day (see Figure H-8). The smallest calibrated fracture permeability of 1.31×10^{-14} m^2 is situated in Column 7, through which the measured maximum infiltration rate is 7.0, which is 17 times less than that in Subplot 11. The calibrated fracture permeability for Column 13 (for the rock mass surrounding the 12 central rock columns) is 1.20×10^{-12} m^2, one order of magnitude larger than the largest calibrated fracture permeability in the central rock columns. Such a difference in calibrated fracture permeability may result from the incapability

of the numerical model to capture flow diversion caused by nonvertical fractures, a discrete feature of fracture network. In such nonvertical fractures, water flows along fracture planes. For a fracture plane with a dip of 81°, the horizontal distance is 3.3 m at a vertical distance of 21.1 m from the liquid-release point. Such a mechanism of water diversion can be handled in the continuum approach only by using strong heterogeneity of rock properties in the lateral direction. The large calibrated fracture permeability for the surrounding rock mass facilitates the lateral water flow from the central columns. The calibrated fracture permeability in the upper unit is in the range of air permeability measured in six 12 m long near-vertical boreholes drilled around the large infiltration plot. The measured air permeability varies over five orders of magnitude, ranging from 3.60×10^{-15} to 6.25×10^{-9} m^2 (BSC 2003a). The geometric mean of the calibrated fracture permeability in the 13 rock columns is 6.31×10^{-14} m^2, which is close to that of the measured air permeability (7.94×10^{-14} m^2). The standard deviation of calibrated log permeability (0.52) is smaller than 1.29 for the measured air permeability because the sampling size for rock columns is larger than the 0.3 m intervals used for measuring air permeability. The calibrated van Genuchten α for Column 13 is twice that of the 12 central rock columns, but the capillary force, caused mainly by the fracture-saturation difference between the surrounding rock mass and the central columns, draws more water away from the central area, leading to water diversion.

In summary, the calibrated fracture permeability in the upper unit reflects the spatial variability in the measured infiltration rates and is consistent with the air permeability data in terms of geometric mean and standard deviation.

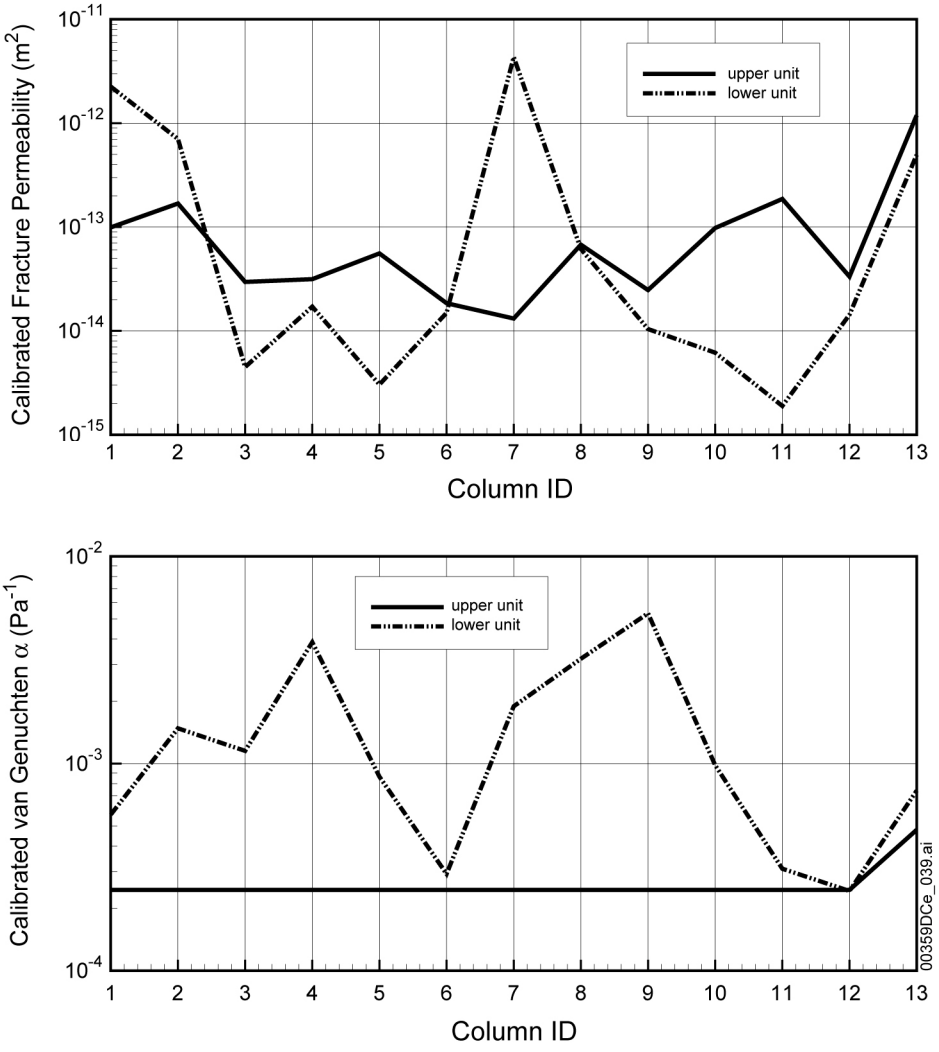

Source: DTN: LB0312A8N3MDLG.002.

Figure H-17. Calibrated Fracture Permeability and α for the Upper and Lower Hydrogeologic Units

Figure H-18 shows a positive correlation between the calibrated fracture permeability used in the continuum approach and the fracture density calculated using the discrete features of the fracture network. This correlation indicates that the fracture permeability partially reflects the spatial variability in discrete fractures within each of the subplots. For example, the largest calibrated fracture permeability is in Column 11, which also has the highest calculated fracture density on its top. However, this positive correlation is not strong, with a correlation coefficient of 0.44. This positive but weak correlation demonstrates the importance of focusing flow (resulting from in-fracture-plane heterogeneity) in single fractures (Dahan et al. 1999) and the importance of the connectivity of water-conducting fractures in fracture networks (Liu et al. 1998; Glass et al. 2002). The calibrated fracture permeability also includes the contributions from small fractures because nonzero infiltration rates were observed for three subplots without large fractures. It is believed that the calibrated fracture permeability represents the actively participating fractures or fracture segments, which are reflected by the measured infiltration rates.

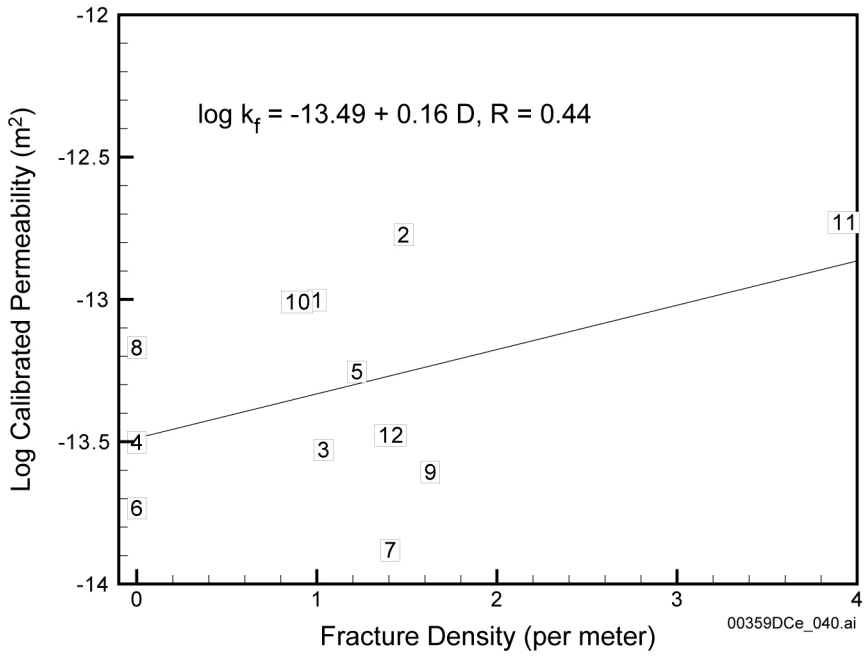

Source: DTNs: LB0312A8N3MDLG.002 (for Calibrated Fracture Permeability) and GS030108314224.001 (for Fracture Density).

Figure H-18. Correlation between Calibrated Fracture Permeability in the Upper Hydrogeologic Unit and Fracture Density on the Floor of Alcove 8

Fracture α is the key parameter affecting the distribution of seepage in space because the difference between fracture and matrix α dominates the exchange of flow between the fracture and matrix continua. The calibrated α in the lower hydrogeologic unit varied over 1.5 orders of magnitude in space, with its log value ranging from −3.62 to −2.27 (see Figure H-17). The mean of log α is −2.97, and the standard deviation is 0.45. In general, the spatial variability in the calibrated fracture α corresponds well to that of measured seepage rate (see Figure H-19). In the x direction (or tray row), the relative α values over several rock columns can be interpreted by the measured seepage rate. For example, the calibrated fracture α values for Columns 3 to 6 in the first tray row demonstrate that a smaller value of α (higher capillary strength) is needed to maintain a higher seepage rate. The measured seepage rate in Tray Unit 6 is the highest among the four columns, and the calibrated α for Column 6 is the lowest. The same situation is true for rock Columns 9 to 12 (Columns 11 and 12 share the same measured seepage rates as those in Tray Unit 11). The smallest α value is obtained for Column 12, where the highest seepage rate was measured in the second row of tray units. The calibrated α is less affected by the difference in the measured seepage rate along the niche axis because of the configuration of tray units. The interaction area between two neighboring columns in the x direction is four times that in the y direction. The calibrated α values for each front–back pair of rock columns in the y direction demonstrate that smaller α value is always obtained for a higher seepage rate. Figure H-19 shows that log (calibrated) α is negatively correlated to the mean seepage rate at later time, with a correlation coefficient of −0.46. Such a correlation is stronger at later time than at early time because of the higher weight factor used in the objective function for the later seepage data and because of the quasi-stable features of measured seepage rates at later time.

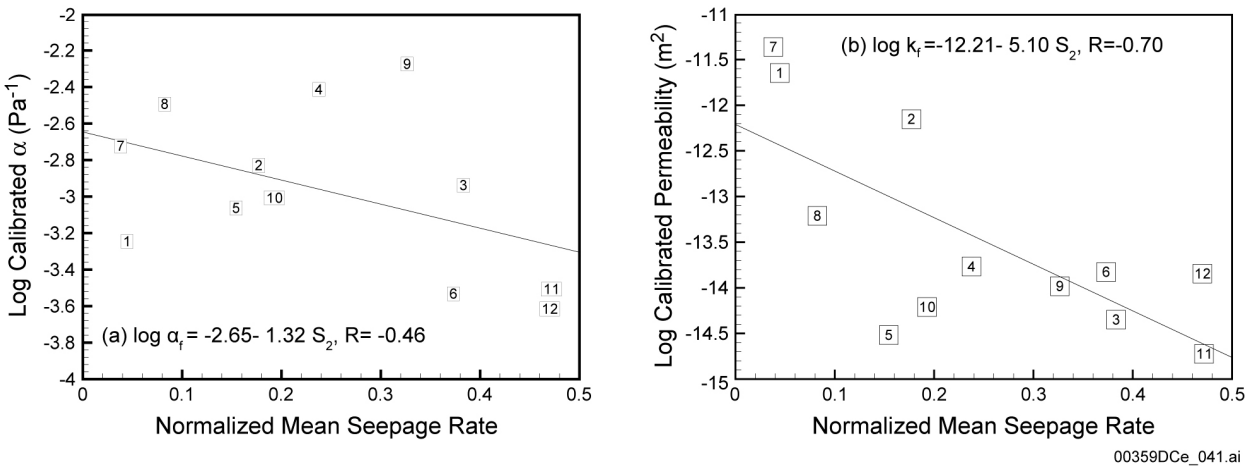

Source: DTNs: LB0312A8N3MDLG.002 (for Calibrated Fracture Permeability and Alpha) and LB0312A8N3MDLG.001 (for Calculating Normalized Seepage Rates).

Figure H-19. Correlations of Calibrated Fracture α and Permeability in the Lower Hydrogeologic Unit with Normalized Seepage Rates Measured on the Niche Ceiling

The calibrated fracture permeability in the lower hydrogeologic unit is also correlated to the measured seepage rates. It varies over three orders of magnitude for the 13 rock columns, ranging from 1.89×10^{-15} to 4.34×10^{-12} m^2. Large calibrated fracture permeability occurs at Columns 1, 2, 7, and 8, where the seepage rate through their corresponding tray units is relatively low. For example, the calibrated fracture permeability for Column 1 is 2.25×10^{-12} m^2, which is the second highest, while the measured seepage rate at early and later time is the lowest. On the other hand, the calibrated fracture permeability for rock columns with high seepage rates at both early and later time is small. For example, the calibrated fracture permeability for Column 12 is 1.43×10^{-14} m^2, but its seepage rate is the second highest at both early and later time. As shown in Figure H-19, calibrated log fracture permeability is well correlated to the mean seepage rates at later time, with a correlation coefficient of −0.70. This high correlation may contradict the concept that water in fractures flows along some preferential flow paths (e.g., large fractures or faults) with high permeability or apertures. The contradictory calibration results may be due to the following considerations. Calibrated fracture permeability for the rock columns with significant seepage rates depends mainly on the transport time of the wetting fronts measured. In the numerical model, both vertical and horizontal connections were used for fracture and matrix continua, with some fracture-matrix connections. Because unsaturated flow is gravity-dominant, the simulated flow rate and transport time depend mainly on fracture permeability. In reality, the connectivity for water-conducting fractures is complicated, and more factors may affect the transport time measured by boreholes and the occurrence of seepage. However, such factors cannot be captured in the mathematical model used in the numerical model. As a result, the calibrated fracture permeability is reasonable in the framework of the numerical model. Linear regression indicates that the calibrated fracture permeability is not correlated with the calibrated van Genuchten α, as assumed in model calibration, in spite of both rock parameters being correlated to the mean seepage rates at later time. This noncorrelation may not affect the calibration results because weaker correlation between permeability and α in the fracture network than in porous media is expected, and the capillary strength in fracture network is much smaller than in porous media.

H.4.4 Summary

In response to the SDS 3.01 AIN-1, a fracture-informed analysis was conducted using the measured infiltration and seepage rates based on the fracture maps on the alcove floor and niche ceiling. The following findings were obtained:

- A positive correlation between measured infiltration rates and calculated fracture density was obtained. The measured infiltration rates reflected the effects of the total actively participating fractures (and fracture segments); the calculated fracture density includes active fractures (and segments) and inactive ones. The positive correlations demonstrate that discrete fractures in the large infiltration plot played a critical role in water percolation. However, the correlations were weakened by in-fracture-plane heterogeneity and complicated dynamic effects. Therefore, capturing discrete features of a fracture network does not mean success in capturing complicated unsaturated flow.

- Lack of correlation between measured seepage rates and calculated fracture density was found at both early and later time. This lack of correlation may indicate that seepage occurs in the form of fragmented and fingered flow in active fractures or in active fracture segments within single fractures, caused by in-fracture-plane heterogeneity. The flow fragmentation and fingers, major features of unsaturated flow in fractured rock under low-flow-rate conditions, may not be a function of fracture trace length represented by fracture density. The lack of correlation also demonstrates the importance of water diversion around Niche 3 caused by small and excavation-induced fractures, capillary barrier layer effects, and film flow on the surface of the niche ceiling. These mechanisms for water diversion around Niche 3 have been found by a series of seepage tests in Niche 3 and other niches.

- The different correlation of infiltration and seepage with mapped large fractures demonstrates the effect of flow rate on unsaturated flow. In the test, the flow transits from pervasive saturated flow (in the vicinity of the large infiltration plot) to the fragmented and fingered unsaturated flow under low-flow-rate conditions (in the lower portion of the system around Niche 3).

- The uncertainties in the fracture network between Alcove 8 and Niche 3 encourages the use of the continuum approach to simulate unsaturated flow. A three-dimensional unsaturated flow model with column-based heterogeneity was developed and calibrated using the measured infiltration and seepage data. The calibrated fracture permeability and van Genuchten α are partially correlated to the density of discrete fractures, indicating that the calibrated rock properties are representative of actively participating fractures. The good match between measured and simulated seepage rates for each of the tray units and the total capture system demonstrate that the numerical model based on the continuum approach can capture the major features of mesoscale unsaturated flow in fractured rock.

In response to USFIC 6.03, reply to NRC staff's eight comments on the Alcove 8–Niche 3 tests and pretest predictions is provided in Section H.3.2. In addition, the methodology for use of all

rock properties available in model calibration is given in Section H.4.3 to resolve Comment 4 on determination of rock properties in model calibration.

Agreement RT 3.05 is related to documentation of Alcove 8–Niche 3 tests and pretest predictions, and can be referred to the response to RT 3.06 in Appendix E of this technical basis document. Appendix E documents the pretest predictions for the Phase I (Stage 3) tracer test using the Phase I (Stage 1) infiltration and seepage data for the large-plot test.

H.5 REFERENCES

H.5.1 Documents Cited

Bear, J.; Tsang, C.F.; and de Marsily, G., eds. 1993. *Flow and Contaminant Transport in Fractured Rock*. San Diego, California: Academic Press. TIC: 235461.

Brocoum, S. 2001a. "Transmittal of Key Technical Issue (KTI) Agreement for Structural Deformation and Seismicity (SDS) KTI." Letter from S. Brocoum (DOE) to C.W. Reamer (NRC), September 28, 2001. ACC: MOL.20011106.0148.

Brocoum, S. 2001b. "Response to Radionuclide Transport Key Technical Issue Technical Exchange Subissue 3, Agreement 6; and Structural Deformation and Seismicity Key Technical Issue Technical Exchange Subissue 3, Agreement 2 with Concurrence Copy–Enclosure not Included, March 12, 2001." Letter from S. Brocoum (DOE) to C.W. Reamer (NRC), March 12, 2001. ACC: MOL.20030922.0008.

BSC (Bechtel SAIC Company) 2003a. *In Situ Field Testing of Processes*. ANL-NBS-HS-000005 REV 02B. Las Vegas, Nevada: Bechtel SAIC Company. ACC: MOL.20030915.0238.

BSC 2003b. *Calibrated Properties Model*. MDL-NBS-HS-000003 REV 01, with errata. Las Vegas, Nevada: Bechtel SAIC Company. ACC: DOC.20030219.0001; DOC.20031014.0011.

BSC 2003c. *Analysis of Hydrologic Properties Data*. MDL-NBS-HS-000014 REV 00. Las Vegas, Nevada: Bechtel SAIC Company. ACC: DOC.20030404.0004.

BSC 2003d. *UZ Flow Models and Submodels*. MDL-NBS-HS-000006 REV 01. Las Vegas, Nevada: Bechtel SAIC Company. ACC: DOC.20030818.0002.

BSC 2004. *Seepage Calibration Model and Seepage Testing Data*. MDL-NBS-HS-000004 REV 02, with errata. Las Vegas, Nevada: Bechtel SAIC Company. ACC: DOC.20030408.0004; DOC.20040202.0003; DOC.20040219.0003.

Cacas, M.C.; Ledoux, E.; De Marsily, G.; Tillie, B.; Barbreau, A.; Durand, E.; Feuga, B.; and Peaudecerf, P. 1990. "Modeling Fracture Flow with a Stochastic Discrete Fracture Network: Calibration and Validation. 1. The Flow Model." *Water Resources Research*, *26*, (3), 479–489. Washington, D.C.: American Geophysical Union. TIC: 222351.

CRWMS M&O (Civilian Radioactive Waste Management System Management and Operating Contractor) 2000. *Fracture Geometry Analysis for the Stratigraphic Units of the Repository Host Horizon.* ANL-EBS-GE-000006 REV 00. Las Vegas, Nevada: CRWMS M&O. ACC: MOL.20000918.0286.

Dahan, O.; Nativ, R.; Adar, M.; Berkowitz, B.; and Ronen, Z. 1999. "Field Observation of Flow in a Fracture Intersecting Unsaturated Chalk." *Water Resources Research*, *35*, (11), 3315–3326. Washington, D.C.: American Geophysical Union. TIC: 255851.

Doughty, C. 1999. "Investigation of Conceptual and Numerical Approaches for Evaluating Moisture, Gas, Chemical, and Heat Transport in Fractured Unsaturated Rock." *Journal of Contaminant Hydrology*, *38*, (1–3), 69–106. New York, New York: Elsevier. TIC: 244160.

Dverstorp, B. and Andersson, J. 1989. "Application of the Discrete Fracture Network Concept with Field Data: Possibilities of Model Calibration and Validation." *Water Resources Research*, *25*, (3), 540–550. Washington, D.C.: American Geophysical Union. TIC: 254736.

Faybishenko, B.; Bodvarsson, G.S.; and Salve, R. 2003. "On the Physics of Unstable Infiltration, Seepage, and Gravity Drainage in Partially Saturated Tuffs." *Journal of Contaminant Hydrology*, *62–63*, 63–68. New York, New York: Elsevier. TIC: 254205.

Finsterle, S. 1999. *ITOUGH2 User's Guide*. LBNL-40040. Berkeley, California: Lawrence Berkeley National Laboratory. TIC: 243018.

Finsterle, S. 2000. "Using the Continuum Approach to Model Unsaturated Flow in Fractured Rock." *Water Resources Research*, *36*, (8), 2055–2066. Washington, D.C.: American Geophysical Union. TIC: 248769.

Finsterle, S.; Ahlers, C.F.; Trautz, R.C.; and Cook, P.J. 2003. "Inverse and Predictive Modeling of Seepage into Underground Openings." *Journal of Contaminant Hydrology*, *62–63*, 89–109. New York, New York: Elsevier. TIC: 254205.

Flint, L.E. 1998. *Characterization of Hydrogeologic Units Using Matrix Properties*, *Yucca Mountain, Nevada*. Water-Resources Investigations Report 97-4243. Denver, Colorado: U.S. Geological Survey. ACC: MOL.19980429.0512.

Glass R.J.; Nicholl, M J.; Ramirez, A.L.; and Daily, W.D. 2002. "Liquid Phase Structure within an Unsaturated Network Beneath a Surface Infiltration Event: Field Experiment." *Water Resources Research*, *38*, (10), 17-1–17-16. Washington, D.C.: American Geophysical Union. TIC: 255850.

Hinds, J.; Bodvarsson, G.S.; and Nieder-Westermann, G.H. 2003. "Conceptual Evaluation of the Potential Role of Fractures in Unsaturated Processes at Yucca Mountain." *Journal of Contaminant Hydrology*, *62–63*, 111–132. New York, New York: Elsevier. TIC: 254205.

Liu, H.-H.; Bodvarsson, G.S.; and Finsterle, S. 2002. "A Note on Unsaturated Flow in Two-Dimensional Fracture Networks." *Water Resources Research*, *38*, (9), 15-1–15-9. Washington, D.C.: American Geophysical Union. TIC: 253307.

Liu, H.-H.; Doughty, C.; and Bodvarsson, G.S. 1998. "An Active Fracture Model for Unsaturated Flow and Transport in Fractured Rocks." *Water Resources Research*, *34*, (10), 2633–2646. Washington, D.C.: American Geophysical Union. TIC: 243012.

Liu, H.-H.; Haukwa, C.B.; Ahlers, C.F.; Bodvarsson, G.S.; Flint, A.L.; and Guertal, W.B. 2003. "Modeling Flow and Transport in Unsaturated Fractured Rock: An Evaluation of the Continuum Approach." *Journal of Contaminant Hydrology*, *62–63*, 173–188. New York, New York: Elsevier. TIC: 254205.

Philip, J.R. 1990. "Some General Results on the Seepage Exclusion Problem." *Water Resources Research*, *26*, (3), 369–377. Washington, D.C.: American Geophysical Union. TIC: 254266.

Pruess, K. and Narasimhan, T.N. 1985. "A Practical Method for Modeling Fluid and Heat Flow in Fractured Porous Media." *Society of Petroleum Engineers Journal*, *25*, (1), 14–26. Dallas, Texas: Society of Petroleum Engineers. TIC: 221917.

Pruess, K.; Oldenburg, C.M.; and Moridis, G. 1999. *TOUGH2 User's Guide, Version 2.0*. LBNL-43134. Berkeley, California: Lawrence Berkeley National Laboratory. TIC: 253038.

Reamer, C.W. 2002. "Radionuclide Transport Key Technical Issue Agreements." Letter from C.W. Reamer (NRC) to S. Brocoum (DOE), February 6, 2002, with attachments. ACC: MOL.20020920.0318.

Reamer, C.W. and Gil, A.V. 2000. *Summary Highlights of NRC/DOE Technical Exchange and Management Meeting on Structural Deformation and Seismicity, October 11-12, 2000, Las Vegas, Nevada*. Washington, D.C.: U.S. Nuclear Regulatory Commission. ACC: MOL.20001102.0042.

Reamer, C.W. and Williams, D.R. 2000a. *Summary Highlights of NRC/DOE Technical Exchange and Management Meeting on Radionuclide Transport*. Meeting held December 5-7, 2000, Berkeley, California. Washington, D.C.: U.S. Nuclear Regulatory Commission. ACC: MOL.20010117.0063.

Reamer, C.W. and Williams, D.R. 2000b. *Summary of Highlights of NRC/DOE Technical Exchange and Management Meeting on Unsaturated and Saturated Flow under Isothermal Conditions*. Meeting held August 16-17, 2000, Berkeley, California. Washington, D.C.: U.S. Nuclear Regulatory Commission. ACC: MOL.20001201.0072.

Salve, R.; Oldenburg, C.M.; and Wang, J.S.Y. 2003. "Fault-Matrix Interactions in Nonwelded Tuff of the Paintbrush Group at Yucca Mountain." *Journal of Contaminant Hydrology*, *62–63*, 269–286. New York, New York: Elsevier. TIC: 254205.

Schlueter, J. 2002. *Structural Deformation and Seismicity Key Technical Issue Agreement, NRC Review of DOE Documents Pertaining to Key Technical Issue Agreements*. Letter from J. Schlueter (NRC) to J.D. Ziegler (DOE), May 21, 2002. ACC: MOL.20020815.0492.

Schlueter, J.R. 2003. "Staff Review of Information Addressing Radionuclide Transport (RT) Agreement 3.06 and Structural Deformation and Seismicity (SDS) Agreement 3.02, Status Partly Received." Letter from J.R. Schlueter (NRC) to J.D. Ziegler (DOE/ORD), February 14, 2003, 0220036149, with attachment. ACC: MOL.20030909.0374.

Su, G.W.; Geller, J.T.; Pruess, K.; and Wen, F. 1999. "Experimental Studies of Water Seepage and Intermittent Flow in Unsaturated, Rough-Walled Fractures." *Water Resources Research*, *35*, (4), 1019–1037. Washington, D.C.: American Geophysical Union. TIC: 245798.

Tokunaga, T.K.; and Wan, J. 1997. "Water Film Flow Along Fracture Surfaces of Porous Rock." *Water Resources Research*, *33*, (6), 1287–1295. Washington, D.C.: American Geophysical Union. TIC: 242739.

Trautz, R.C. and Wang, J.S.Y. 2002. "Seepage into an Underground Opening Constructed in Unsaturated Fractured Rock Under Evaporative Conditions." *Water Resources Research*, *38*, (10), 6-1–6-14. Washington, D.C.: American Geophysical Union. TIC: 253348.

van Genuchten, M.T. 1980. "A Closed-Form Equation for Predicting the Hydraulic Conductivity of Unsaturated Soils." *Soil Science Society of America Journal*, *44*, (5), 892–898. Madison, Wisconsin: Soil Science Society of America. TIC: 217327.

Wang, J.S.Y. and Bodvarsson, G.S. 2003. "Evolution of the Unsaturated Zone Testing at Yucca Mountain." *Journal of Contaminant Hydrology*, *62–63*, 337-360. New York, New York: Elsevier. TIC: 254205.

Williams, N H. 2001. "Contract No. DE-AC08-01RW12101 – Transmittal of Methodology for Three-Dimensional Depiction of Fractures between Alcove 8 & Niche 3." Letter from N.H. Williams (DOE) to S.J. Brocoum (NRC), November 19, 2001, with enclosure. ACC: MOL.20020115.0031.

Zhou, Q.; Liu, H.-H.; Bodvarsson, G.S.; and Oldenburg, C.M. 2003. "Flow and Transport in Unsaturated Fractured Rock: Effects of Multiscale Heterogeneity of Hydrogeologic Properties." *Journal of Contaminant Hydrology*, *60*, (1–2), 1–30. New York, New York: Elsevier. TIC: 253978.

Ziegler, J.D. 2002. "Transmittal of Information Addressing Key Technical Issue (KTI) Agreement Items Radionuclide Transport (RT) 3.06 and Structural Deformation and Seismicity (SDS) 3.02." Letter from J.D. Ziegler (DOE/YMSCO) to J.R. Schlueter (NRC), June 27, 2002, OL&RC:TCG-1316, 0628023167, with attachment. ACC: MOL.20020819.0283.

H.5.2 Data, Listed by Data Tracking Number

GS030108314224.001. Geotechnical Data for Alcove 8 (ECRB) and Niche 3 (ESF): Full Periphery Geologic Map (Drawing OA-46-356). Submittal date: 02/05/2003.

GS030608312242.005. Surface Infiltration in a Large Plot in Alcove 8 Using Permeameters (11/19/2002–3/24/2003). Submittal date: 06/24/2003.

LB0306A8N3LIQR.001. Fault Infiltration Test From Alcove 8 to Niche 3 (9/18/2002–10/16/2002). Submittal date: 06/19/2003.

LB0308A8N3TRTM.001. Seepage Travel Times in Niche 3 (9/4/02–3/29/03). Submittal date: 08/29/2003.

LB0312A8N3MDLG.001. Pre-Test Prediction Results For Alcove 8/ Niche 3: Simulations. Submittal date: 12/17/2003.

LB0312A8N3MDLG.002. Pre-Test Prediction Results For Alcove 8/ Niche 3: Data Summary. Submittal date: 12/17/2003.